

On the Uncertainties of Stellar Mass Estimates via Colour Measurements

Joel C. Roediger^{1,2,3} and Stéphane Courteau¹

¹ *Department of Physics, Engineering Physics & Astronomy, Queen's University, Kingston, Ontario, Canada*

² *Department of Astronomy & Astrophysics, University of California, Santa Cruz, CA, USA*

³ *National Research Council of Canada, Victoria, BC, Canada*

Joel.Roediger@nrc-cnrc.gc.ca, courteau@astro.queensu.ca

ABSTRACT

Mass-to-light versus colour relations (MLCRs), derived from stellar population synthesis models, are widely used to estimate galaxy stellar masses (M_*) yet a detailed investigation of their inherent biases and limitations is still lacking. We quantify several potential sources of uncertainty, using optical and near-infrared (NIR) photometry for a representative sample of nearby galaxies from the Virgo cluster. Our method for combining multi-band photometry with MLCRs yields robust stellar masses, while errors in M_* decrease as more bands are simultaneously considered. The prior assumptions in one's stellar population modelling dominate the error budget, creating a colour-dependent bias of up to 0.6 dex if NIR fluxes are used (0.3 dex otherwise). This matches the systematic errors associated with the method of spectral energy distribution (SED) fitting, indicating that MLCRs do not suffer from much additional bias. Moreover, MLCRs and SED fitting yield similar degrees of random error (~ 0.1 - 0.14 dex) when applied to mock galaxies and, on average, equivalent masses for real galaxies with $M_* \sim 10^{8-11} M_\odot$. The use of integrated photometry introduces additional uncertainty in M_* measurements, at the level of 0.05-0.07 dex. We argue that using MLCRs, instead of time-consuming SED fits, is justified in cases with complex model parameter spaces (involving, for instance, multi-parameter star formation histories) and/or for large datasets. Spatially-resolved methods for measuring M_* should be applied for small sample sizes and/or when accuracies less than 0.1 dex are required. An Appendix provides our MLCR transformations for ten colour permutations of the *grizH* filter set.

Subject headings: galaxies: clusters: individual: Virgo; galaxies: general; galaxies: formation; galaxies: fundamental parameters; galaxies: stellar content

1. Introduction

Stellar mass (M_*) is one of the most fundamental parameters for tracing the formation of galaxies, as embodied in its many correlations with other galaxy properties, such as halo mass, size, star formation rate, gas-phase and stellar metallicity, at all redshifts (Tremonti et al. 2004; Gallazzi et al. 2005; Behroozi et al. 2010; Mannucci et al. 2010). Knowledge of M_* also informs us on a variety of phenomena pertaining to galaxy formation efficiencies, dynamics, and feedback histories. Given its astrophysical relevance, there is natural interest in measuring M_* as accurately as possible, whilst also achieving a complete account of its associated errors.

For local galaxies, whose distances are fairly well-known, determining M_* essentially consists of measuring the mean mass-to-light ratio (M_*/L) of their stellar populations. The standard approach of measuring M_*/L is to fit stellar population synthesis (SPS) models to the SED, line strength indices, and/or full spectrum of a galaxy. Alternatively, one may access M_*/L through maximal-disk fits (e.g. van Albada & Sancisi 1986), relations between M_*/L and broadband colour (e.g. Bell et al. 2003), or a combination of the two (Bell & de Jong 2001). These methods allow one to access M_*/L whenever multi-band photometry or high-quality spectroscopy is unavailable.

In addition to minimal input, M_*/L -colour relations (MLCRs) make determining mass-to-light ratios quite trivial, through the use of (quasi-)linear relations. The linearity of MLCRs stems from the fact that changes in age, metallicity, and reddening scatter model stellar populations along the relations rather than away from them; equivalently, the age-metallicity-reddening degeneracy conspires to keep the scatter in MLCRs low (Bell & de Jong 2001). The simplicity of MLCRs has precipitated their widespread use, as well as several calibrations of these relations (Bell & de Jong 2001; Bell et al. 2003; Zibetti et al. 2009; Gallazzi & Bell 2009; Taylor et al. 2011; Into & Portinari 2013; McGaugh & Schombert 2014) [hereafter BdJ01, B03, GB09, Z09, T11, IP13, and MS14 respectively]. These calibrations differ largely by virtue of their underlying SPS treatments, including the effects of dust attenuation, bursts of star formation and chemical evolution. These effects can also be modelled via other methods for measuring M_*/L (e.g. SED fitting), though usually at the cost of increased computational expense. The MLCR method suffers no such penalty for added model complexity though, making it an expedient, and thus practical (if reliable), route to M_*/L in most circumstances.

Despite their widespread use, an exhaustive analysis of the accuracy of MLCRs is still lacking (GB09 being the most in depth thus far). BdJ01 showed that uncertainties in their adopted treatments of SPS, galaxy evolution, and dust translated into a wavelength-dependent error of 0.1-0.2 dex in M_*/L while large bursts of recent star formation (10% by mass) inflate this range to 0.3-0.5 dex. Although B03 echoed these conclusions, the BdJ01 MLCRs targeted spiral galaxies alone (as did MS14) and the B03 MLCRs excluded treatments for reddening and bursts of star formation. Z09 argued that omitting the latter effects results in systematically larger M_*/L values at

blue colours and smaller values at red colours. Using mock galaxies, GB09 studied a multitude of effects on the recovery of M_*/L , finding, amongst other things, that with sufficient signal-to-noise (S/N ; >30), individual optical colours performed as well as spectroscopic indices in the median, except for galaxies described intermediate-age populations and a bursty star formation history (SFH).

To be sure, effects other than our assumptions about the SFHs and dust contents of nearby galaxies contribute to the uncertainty budget underlying MLCRs. Z09 compared MLCRs derived from the Bruzual & Charlot (2003, hereafter BC03) SPS model and the unpublished 2007 update thereof (hereafter CB07), where the greatest difference between the two presumably lay in their prescriptions for TP-AGB stars. They demonstrated that this phase of stellar evolution alone can alter M_*/L predictions by up to 0.1 and 0.4 dex at optical and near-infrared (NIR) wavelengths, respectively. T11 partly explored the effect of constraining MLCRs with SED fits to real galaxies. While their empirical MLCR differs markedly in shape from the one defined by their prior-weighted SPS model library (see their Fig. 13), the two appear to be statistically consistent everywhere except in the interval $g-i = 0.7-1.05$. MS14 presented corrections to several sets of published MLCRs (including B03, Z09, and IP13) for inconsistencies in predicted M_*/L throughout the optical-NIR wavelength range, presumably tied to uncertainties in stellar evolution, although the corrections were solely based on a limited sample of nearby spiral galaxies and the degree of inconsistency was not quantitatively established. Finally, the choice of IMF is a crucial parameter of MLCRs as it controls their normalisations (zero-points). For example, M_* estimates based on a Chabrier or Salpeter IMF differ by 0.3 dex, with the latter being higher.

Most, if not all, of the systematics inherent to the MLCRs have also been studied in the context of SED fitting, all yielding similar results. While much effort has been spent on understanding the latter (see Conroy 2013 and Courteau et al. 2014 for recent reviews), the computational expense associated with even modest parameter spaces severely complicates the investigation of certain issues via SED fitting. For instance, masses derived from integrated photometry are biased to the brightest regions within galaxies (i.e. light-weighted) and therefore susceptible to erroneous M_*/L determinations. Two clear causes of this are interstellar dust or bright stars, which can shroud or outshine a potentially large fraction of a galaxy’s stellar mass. This bias can be overcome by adding up the mass in galaxies pixel-by-pixel. Given the many pixels that local galaxies fill with modern imaging cameras, measuring M_* pixel-by-pixel through SED fits is potentially expensive. Thus in their study of spatially-resolved stellar masses, Z09 drew on the MLCR method. They found that the pixel-by-pixel approach yields masses that are larger than their integrated counterparts by up to 0.2 dex, depending on the filters and SPS models used. The Z09 sample however was small (9 galaxies) and skewed to late-type spirals (5/9 had Sbc/Sc morphologies). An expanded sample

would cement their findings on firmer grounds¹

We wish to address several open issues pertaining to MLCRs for the measurement of M_* . While earlier studies have focussed on comparisons of theoretical MLCRs against one another for various combinations of colours and M_*/L_X (the mass-to-light ratio in filter X), we also take the approach of comparing them against *real* galaxies. To this end, we conduct several tests of MLCRs using a representative sample of local galaxies drawn from the “SHIVir survey” of Virgo Cluster galaxies, for which deep luminosity profiles at optical and NIR wavelengths are available (McDonald et al. 2011). We also consider *multiple* colours at once in fitting for M_*/L , whereas previous analyses used two colours at most (Z09). We specifically address M_* differences due to: (i) MLCRs versus SED fitting; (ii) different MLCR sets; (iii) limited SED constraints; and (iv) integrated versus spatially-resolved photometric data.

Our paper is organized as follows. In Section 2, we introduce the SHIVir survey upon which our stellar masses are derived. In Section 3, we construct our own MLCRs, including a discussion of our assumed priors, and test the fidelity of SED-based masses using mock galaxies, which allows us to rank the systematics inherent to the MLCR method. The latter are investigated and quantified (using real galaxies) in Section 4. Finally, our conclusions and suggestions for future work are reported in Section 5.

2. Data

Thanks to its proximity and richness, the Virgo Cluster enables the simultaneous analysis of the stellar populations in all types of present-day galaxies on both spatially-resolved and integrated scales. The SHIVir survey (“Spectroscopy and H -band Imaging of Virgo cluster galaxies”; McDonald et al. 2011) seizes this opportunity by combining optical and NIR imaging for a volume-limited sample of Virgo galaxies with apparent B -band magnitudes > 16 and located $\lesssim 1.7$ Mpc (in projection) from the core of the sub-cluster A, taken to be M87. Like the cluster itself, the sample includes the full range of morphological types and is thus representative of the low-redshift galaxy population. For these reasons, we draw on the SHIVir survey for our tests of the MLCR method.

The SHIVir galaxies were imaged in four optical filters ($griz$) and the NIR H -band. The optical imaging was downloaded from the seventh data release of the Sloan Digital Sky Survey (SDSS;

¹During the final review of this paper, the manuscript by (Sorba & Sawicki 2015, hereafter SS15) expanded upon Z09’s findings by measuring pixel-by-pixel masses for 67 nearby galaxies comprising 9 E/S0’s, 4 Irr’s and the rest spirals. SS15 stated that the discrepancy between resolved and integrated masses grows with higher specific star formation rates and disappears for spatial resolutions ≥ 3 kpc.

Abazajian et al. 2009). Conversely, the NIR imaging is a heterogeneous collection obtained from either the GOLDMine database (Gavazzi et al. 2003), Two Micron All Sky Survey (2MASS; Skrutskie et al. 2006), or an extensive observational campaign conducted by our team with Mauna Kea telescopes and detectors. SHIVir data products include luminosity profiles, integrated magnitudes, effective radii and surface brightnesses, and concentrations for 286 Virgo cluster galaxies in the *grizH* filters. Further details about SHIVir photometry and its associated data products can be found in McDonald et al. (2009, 2011) and at this website².

3. Modelling the Stellar Mass-to-Light Ratio

We present our adopted method for modelling the stellar mass-to-light ratios of SHIVir galaxies (Section 3.2). Recall that a major aim of this work is to assess whether M_* derived from integrated photometry are consistent with those based on spatially-resolved data. Since the latter typically involve modelling M_*/L for thousands of pixels per galaxy, our method invariably draws upon MLCRs for their expediency. Although several calibrations of MLCRs already exist in the literature (B03, Z09, T11, IP13), our experiment calls for the development of our own MLCRs, as argued below (Section 3.2). We also develop in Section 3.1 mock galaxy tests for the recovery of M_* based on SED fitting. Finally, in Section 3.3 we outline our approach to measuring M_* through 1D light profiles and 2D maps of the stellar mass density (Σ_*) distribution in SHIVir galaxies.

3.1. Mock Galaxy Tests of SED Fitting

This work focusses, in part, on modelling M_* for a representative sample of local galaxies whose light (and thus mass) can be measured in three ways that we refer to as 0D, 1D, and 2D. ‘0D’ refers to the end point of a galaxy curve of growth, i.e. the total luminosity of the galaxy up to a certain radius. ‘1D’ refers to the profile of galaxy surface brightness as a function of galactocentric radius; the brightness at each radius represents the median flux divided by the area subtended by the associated isophote. Lastly, ‘2D’ stands for the 2-dimensional image of a galaxy whose pixels reveal information about the local stellar population.

The principal unknowns governing M_*/L for any stellar population are its IMF, age, metallicity (Z), and reddening. Given the wide range of scales explored in this work, our modelling must therefore include populations covering a variety of evolutionary states. Specifically, we require a library of theoretical stellar populations spanning extensive ranges in star formation rates and

²See also <http://www.astro.queensu.ca/virgo>.

histories, chemistries, and dust contents.

The MAGPHYS library (**M**ulti-wavelength **A**nalysis of **G**alaxy **P**HYSical Properties; da Cunha et al. 2008) is well-suited for our purposes. This library consists of 50,000 randomly-generated stellar and dust emission SEDs that can be self-consistently linked to interpret UV through sub-mm imaging of galaxies in terms of their stellar population and ISM properties. We disregard the dust emission SEDs since constraining ISM properties is not our current concern. Assuming that dust emits at wavelengths $\geq 2.5 \mu\text{m}$, we use only UV-NIR SED information from MAGPHYS. This wavelength range comfortably captures the baseline spanned by the SHIVir database.

The MAGPHYS stellar SEDs can be computed based on either the BC03 or CB07 SPS models. These SEDs are computed according to SFHs prescribed by five parameters. These are the start time (1) and exponential decay rate (2) of continuous star formation, as well as the ages (3), durations (4), and mass fractions (5) of superimposed bursts, if any. No prior constraints are made as to the number of bursts that underlie any given SED other than that half of them reflect a burst that occurred within the past 2 Gyr.

Attenuation is folded into the stellar SEDs following the Charlot & Fall (2000) two-component model for dust in molecular clouds and the ambient ISM. The amount of attenuation suffered by each SED is described by two parameters: the total optical depth towards stars < 0.01 Gyr-old and the fractional contribution of ambient dust to that optical depth (μ). The SED metallicities are also allowed to cover the range $Z = 0.0004$ - 0.04 (i.e. 0.02 - $2 Z_{\odot}$). Altogether, eight parameters are used to describe the stellar SEDs. To compute each SED, the MAGPHYS software randomly draws values of these parameters from prior distributions. See da Cunha et al. (2008) for more information about these priors.

The extensive parameter space covered by the MAGPHYS library encapsulates the variety of stellar populations within present-day galaxies. Accordingly, this library may be used to evaluate the accuracy of M_* measurements from SED fitting. Specifically, we wish to know the effects that S/N and SED sampling have on these measurements. Using mock datasets from MAGPHYS, da Cunha et al. (2008) were able to recover input stellar masses with very high fidelity in the case of an exquisitely sampled SED (i.e. UV through sub-mm fluxes) and a fixed uncertainty of 10% in each filter. The authors also claimed that the masses measured from the integrated SEDs of three galaxies (NGC 0337, 3521; Mrk 33) remained relatively robust even as UV, Balmer, far-IR and sub-mm fluxes were iteratively excluded from their fits. These results, however, were not quantified. Moreover, the authors did not quantify the variations of their M_* estimates if their only available data consisted of optical plus NIR fluxes, a situation that we face here and often encountered in the literature.

To assess the quality of stellar masses that can be achieved with optical and NIR photometry, we have conducted our own mock galaxy tests for various combinations of S/N and SED sampling. For each test, 500 randomly selected MAGPHYS stellar SEDs had Gaussian noise of a fixed percentage applied to their fluxes from a select filter suite. Stellar masses were then measured from these perturbed SEDs using the Bayesian fitting software included in the MAGPHYS package.

Figure 1 demonstrates the accuracy to which MAGPHYS can recover M_* for galaxies and how that accuracy might vary with galaxy parameters. The parameters studied include mass-weighted age, metallicity, ISM optical depth and age of the most recent burst of star formation (t_{burst}). Results are shown for four cases: (i) SEDs perturbed by 10% noise and sampled with the GALEX FUV and NUV , SDSS $ugriz$, and 2MASS H filters [blue points]; (ii) as in (i) but with 5% noise [red]; and (iii) as in (ii) but with SED sampling restricted to the $grizH$ filters [green]; or (iv) using gi filters only [orange]. Cases (i) and (ii) in Fig. 1 reflect the situation of a well-sampled stellar SED while cases (iii) and (iv) match the data available from the SHIVir survey. Case (iv) examines the impact of removing r -, z -, and H -band data, on account of the nebular contamination, low S/N , and/or poor sky subtraction that sometimes compromises galaxy photometry at those wavelengths.

In all four cases, the masses recovered by SED fitting are described by a residual distribution having zero mean and dispersion of 0.09-0.13 dex, i.e. random errors of 23-30%. The robustness of the residuals in Fig. 1 is remarkable given the wide range in data richness explored. We expect that the constraints from well-sampled SEDs should better differentiate themselves from those of coarser SEDs as the S/N increases beyond what we have explored. Furthermore, accuracies of ~ 0.1 dex can be achieved with the SHIVir filters and $S/N = 20$. Such a threshold S/N translates into flux and colour errors of ~ 0.05 mag and ~ 0.10 mag, respectively. The latter error will guide the construction of our own MLCRs, described in the following section.

Fig. 1 also hints at a possible, but complex, trend in accuracy with burst age, whereby masses are maximally overestimated around $t_{\text{burst}} \sim 1-2$ Gyr and underestimated at the youngest and oldest t_{burst} (exclusive of t_{burst}). This trend is consistent with the results of GB09, who found that, for an error of 0.1 mag in $g-i$, the M_*/L of mock galaxies described by bursty SFHs and young/intermediate-age populations have predicted masses with median residuals of 0.0/0.15 dex. It is worth noting that the trend appears weaker for the red points, which have higher S/N . These results suggest that bursts are poorly constrained with broadband photometry of marginal quality ($S/N \leq 10$), no matter how many filters one has data for. Further work aimed at addressing the combination of filters (including narrow bands) and S/N required to unravel the contribution of bursts to the recent SFHs of galaxies would be useful.

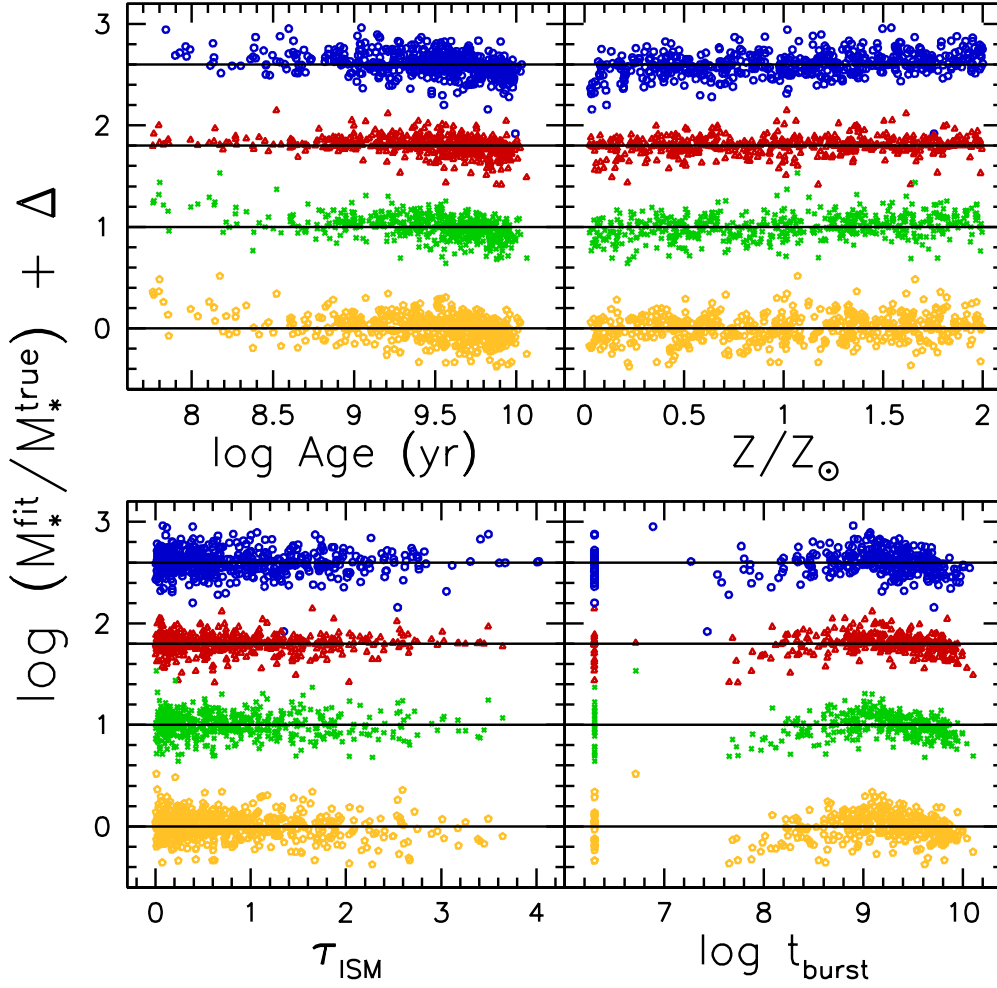


Fig. 1.— Recovery of the known stellar masses (M_*) of 500 mock galaxies via Bayesian SED modeling [$M_*^{\text{fit}} =$ fitted M_* ; $M_*^{\text{true}} =$ true M_*], plotted as a function of mass-weighted age, total metallicity (Z/Z_\odot), ISM optical depth (τ_{ISM}) and age of the latest burst of star formation (t_{burst}). The galaxies were drawn from and fitted with the MAGPHYS library, based on the Bruzual & Charlot (2003, hereafter BC03) stellar population synthesis (SPS) model. The experiment is carried out for four combinations of SED sampling and signal-to-noise ratio (S/N): (a) UV to near-infrared coverage and $S/N = 10$ (blue points); (b) as in (a) but $S/N = 20$ (red); (c) SDSS *griz* + 2MASS *H*, $S/N = 20$ (green); and (d) SDSS *gi* (orange), $S/N = 20$. The filter combinations examined in cases (c-d) focus on the data available from the SHIVir survey (McDonald et al. 2011). Datasets (a-c) have been offset vertically for display purposes (denoted by the solid lines). Galaxies which have experienced a burst during the most recent timestep (i.e. $t_{\text{burst}} = 0.0$) have been assigned to $\log t_{\text{burst}} = 6.3$, also for display purposes. The residual distribution is similar in all cases, having a mean of roughly zero and dispersion of ~ 0.1 dex.

3.2. Estimating M_*/L via Colour Information

In Section 3.1, we quantified the internal accuracy of M_* measurements from SED fitting. This provides us with a benchmark to evaluate the relative success of our adopted method (MLCRs) for measuring M_*/L (Section 4.1). As stated earlier, the appeal of MLCRs lies in their minimal data requirements and expediency in all applications.

Since the pioneering work of Bdj01 and B03, MLCRs have been a popular tool for measuring M_*/L . Similar to the strategies of Z09, GB09, and MS14, we do not restrict our modelling to a single colour. The motivation for this stems from the fact that every colour has a unique pattern of sensitivities to the parameters that determine M_*/L . As a result, the MLCR for any colour contains scatter (T11), which should be accounted for by modelling multiple colours at once. However, using all of the $N(N-1)/2$ colours that may be measured from an SED sampled with N filters would implicitly weigh certain parts of the SED more than others. Moreover, modelling all possible colours at once is tantamount to overfitting the data. For any given SED then, we only consider as many colours as are necessary, when paired with the flux in a single band, to reconstruct the original SED³. We select those colours whose MLCRs have the least amount of scatter; that is, those which are in principle the strongest discriminants of M_*/L . The fact that we can model several colours at once makes our approach unique from those of Z09, GB09, and MS14, each of which considered two colours at most.

Figure 2 highlights our multi-MLCR method for measuring M_*/L . We show with black lines theoretical trends in median M_*/L_i versus all ten colours that can be measured from the full SHIVir SED. These trends were determined from the BC03 version of the MAGPHYS library. The grey lines trace the 16th and 84th percentiles of the model distribution for each MLCR, which we take to be the $1-\sigma$ uncertainty in M_*/L_i . The red lines indicate the M_*/L_i values that we would infer for a random MAGPHYS model according to its integrated *grizH* SED. The MLCRs for $g-r$, $g-i$, $g-z$, and $g-H$ provide the tightest constraints on M_*/L_i for an SED sampled with those filters, and so are the ones that we would use in this case; hence the solid red lines in those panels while all the others are dotted. Comparisons of the M_*/L_i values inferred for SHIVir galaxies based on these colours confirms that, on average, they are mutually consistent within 1σ . Thus by comparing a set of measured colours – be it for an individual pixel, isophote, or whole galaxy – to such MLCRs as displayed in Fig. 2, we can deduce a corresponding set of M_*/L_i measurements. These in turn may be combined to obtain a single M_*/L_i value for the object in question. We use a weighted average, based on the 16-84th percentile range (linear scale), in order to reduce

³The fact that a flux is required to turn M_*/L into M_* means that the number of colours needed to reconstruct a given SED is minimized. For instance, a *grizH* SED is fully described by the *i*-band flux plus the colours $g-r$, $g-i$, and $g-H$.

the contribution from colours that are poorer M_*/L_i discriminants. This is how we use multiple MLCRs simultaneously to measure M_*/L .

A potential pitfall of our method is that, in trying to minimize the random error, we increase the systematic error above the level incurred were we to use MLCRs with larger scatter instead. To show that this is in fact not the case, we plot in Figure 3 the mean offset of the MLCR-based M_*/L_i values predicted from each of the 10 colours accessed by the SHIVir dataset as a function of the mean scatter in the associated MAGPHYS/BC03 MLCRs. The offsets are computed with respect to the M_*/L_i inferred from fitting the *grizH* SEDs with the same model library. The figure convincingly demonstrates that, despite a couple of outliers, there is a clear correlation between the two variables. In other words, the precision of a given MLCR is, on average, directly related to the accuracy of its predictions and our method is physically sound. We have also investigated the impact of folding systematic errors through our mock galaxy tests (Fig. 1) into our weighting scheme and found them to be minimal.

To apply our method to SHIVir data, we require MLCRs cast in terms of both the SDSS and 2MASS/*H* bands. Existing MLCRs prove inadequate for our purposes because they either do not treat both optical and NIR colours (e.g. Z09) or they are based on simplistic priors (e.g. B03). We also wish to measure M_* through Σ_* profiles and maps, in which case our MLCRs must incorporate SFHs that are generally not smooth. Finally, our desire to encompass all morphologies, as in SHIVir, favors MLCRs that span a wide variety of stellar populations. For these reasons, we derived our own MLCRs, based on the MAGPHYS stellar SEDs.

We calibrate our MLCRs in terms of M_*/L_i and all possible colour combinations formed from the *grizH* filters. Although NIR wavelengths are often viewed as yielding the most robust M_*/L values (e.g. Bdl01), the current uncertainties in NIR fluxes predicted for TP-AGB stars make us favour an optical band instead (Maraston 2005; Bruzual 2007). For each relevant colour, we calibrate the associated MLCR with the MAGPHYS/BC03 library in the following way. First, M_*/L_i and the colour of interest are computed for each SED in the library, where the former is based on the present-day M_* . Those SEDs are then grouped by this colour into 0.1 mag-wide bins. The median plus the 16th and 84th percentiles of the M_*/L_i distribution in each bin are then calculated, where the percentiles are used to approximate the $\pm 1\text{-}\sigma$ uncertainties. This straightforward procedure yields the desired MLCR. Note that the choice of bin width was made based on Fig. 1, which shows that optical-to-NIR SEDs having $S/N = 20$ yield stellar masses of comparable accuracy to those with better sampling. Furthermore, surface brightness measurements with $S/N \geq 20$ may be achieved in the outskirts of galaxies through, e.g., isophotal fitting. For colours having errors >0.1 mag, we adjust the $1\text{-}\sigma$ uncertainties on their M_*/L_i measurements to reflect the 16th and 84th percentiles of the bins in which their lower and upper limits fall, respectively. Although our approach to such cases favours larger uncertainties, a more accurate treatment would introduce

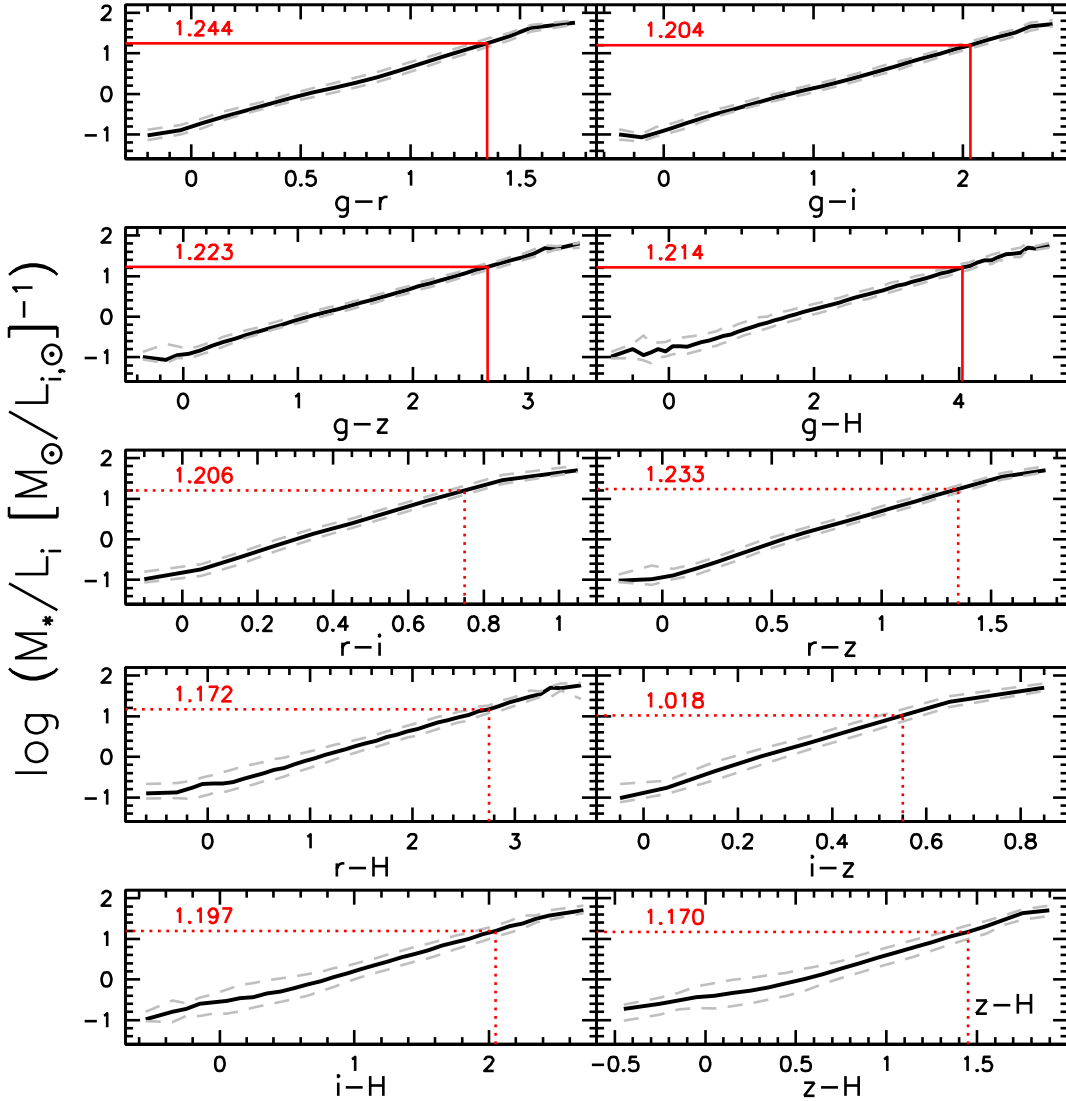


Fig. 2.— Demonstration of the simultaneous use of multiple colours to constrain the stellar mass-to-light ratio (M_*/L) via M_*/L -colour relations (MLCRs; constructed using the MAGPHYS/BC03 library). The black line in each panel traces the median M_*/L_i as a function of the particular colour plotted along the x -axis, while the gray lines indicate the 16th and 84th percentiles. Here we focus on the colours that can be measured for galaxies with the SHIVir dataset. Red lines mark the M_*/L_i values that would be measured for a hypothetical population, given its integrated $grizH$ SED. Since four colours plus the i -band flux is the minimum amount of information required to uniquely describe such an SED, we differentiate the red lines into solid/dotted types according to those colours that provide the strongest/weakest constraints on M_*/L_i . Our procedure then combines the strongest estimates via a weighted average to obtain the overall M_*/L_i for the population in question. While this demo is based on integrated data, it is straightforward to generalize our procedure to work with colour profiles/maps instead.

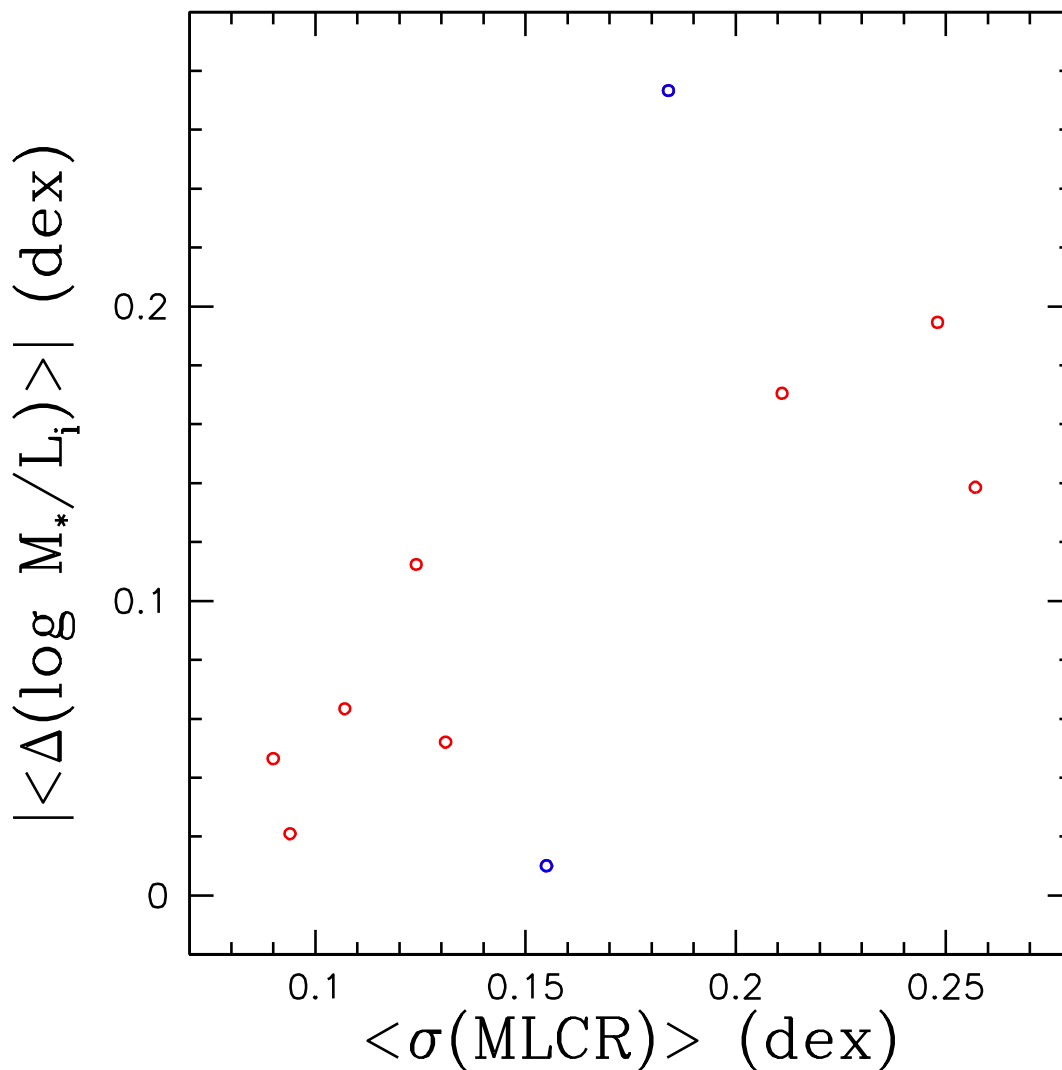


Fig. 3.— Absolute mean offset of M_*/L_i predicted by MLCRs versus the mean scatter in the relations. Each data point corresponds to a colour that can be accessed by the SHIVir survey (e.g. $g-i$) and the value along the vertical axis represents an average over the 280 galaxies contained therein. Offsets were measured with respect to the M_*/L_i determined by fitting the $grizH$ SEDs of the SHIVir galaxies directly. Aside from a couple outliers, there is a clear correlation between the two variables, implying that the precision of a given MLCR is related to its accuracy.

precisely the type of computational intensity we wish to avoid with our method.

3.3. Stellar Mass Density Profiles and Maps

Fig. 2 demonstrates how MLCRs reduce the measurement of M_* to a trivial algorithm. This defining aspect of the MLCR method makes it highly desirable when considering, say, SED modelling for hundreds of thousands of resolution elements per galaxy. Recall that the motivation to compute M_* from 2D maps stems from Z09’s finding (corroborated by SS15) that the mass assessment is more accurate that way.

We now describe the additional preparations to infer M_* for galaxies based on either multi-band luminosity profiles or full images. Note that we shall refer to masses derived from integrated luminosities, surface brightness profiles, and images as M_*^{0D} , M_*^{1D} , and M_*^{2D} , respectively.

For the purpose of comparing these various sets of masses, it is crucial that they be measured at a common galactocentric radius. We choose the i -band 23.5 mag arcsec⁻² isophotal radius ($R_{23.5,i}$) since it and the enclosed light ($m_{23.5,i}$) yield the tightest scaling relations (Hall et al. 2012) and are good proxys for the total sizes and luminosities of galaxies of intermediate-to-high surface brightnesses. This is demonstrated in the top panel of Figure 4, which plots $m_{23.5,i}$ against the extrapolated magnitude in the same band ($m_{tot,i}$) for the SHIVir galaxies. The former were extracted from the SHIVir surface brightness profiles, while the latter were measured by McDonald et al. (2011). The points have been colour-coded by galaxy concentration and the solid black lines mark equality. Three-quarters of the SHIVir sample have $(m_{23.5,i} - m_{tot,i}) < 0.3$ mag, defined by high and intermediate surface brightness galaxies, while departures from $m_{23.5,i} \sim m_{tot,i}$ grow towards lower surface brightnesses, as shown in the bottom panel of Fig. 4. Since our main concern in this work is whether multiple colour measurements can be used to reliably constrain M_*/L , these departures should not affect any of our conclusions.

3.3.1. M_*^{0D} & M_*^{1D}

Since our methods for measuring M_*^{0D} and M_*^{1D} of a galaxy are intertwined, we shall discuss both herein. Both approaches begin with the *grizH* light profiles from SHIVir. Depending on the bands being modelled, we interpolate the profiles (locally) for each galaxy to the largest pixel scale therein. No interpolation is required when modelling optical SEDs alone, since the original data come from a single source (SDSS; pixel scale = 0.396"). On the other hand, the heterogeneous nature of the NIR imaging – having pixel scales in the range = 0.25-1.61" – imply that either those or the optical profiles must be interpolated to a common scale when optical-NIR SEDs are

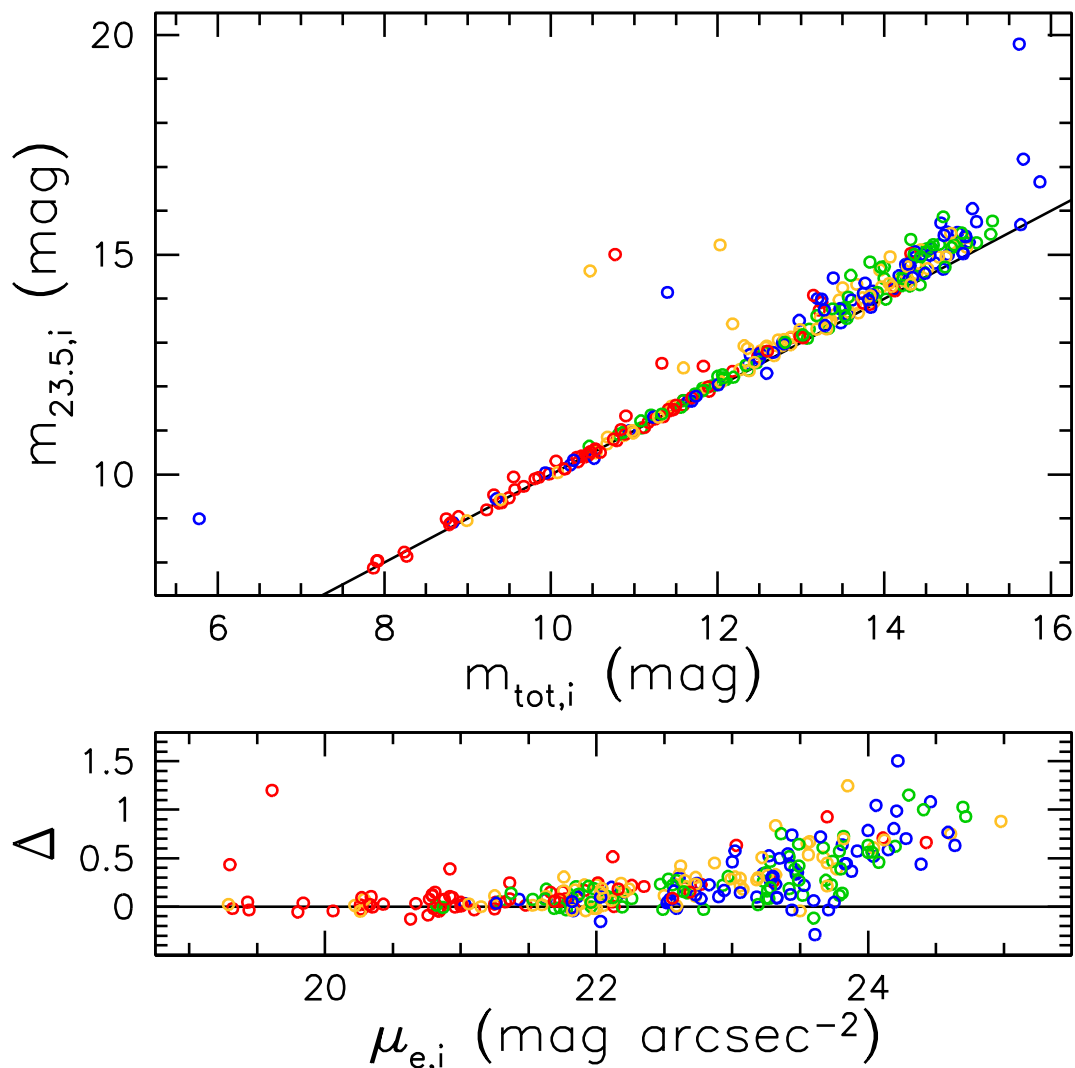


Fig. 4.— (top) Comparison of i -band aperture and extrapolated magnitudes ($m_{23.5,i}$ and $m_{tot,i}$) for SHIVir galaxies, where the former have been measured at the 23.5 mag arcsec⁻² isophotal radius. The points are colour-coded according to galaxy concentration, C_{28} [$C_{28} < 2.86$ (blue), $2.86 \leq C_{28} < 3.31$ (green), $3.31 \leq C_{28} < 3.99$ (orange), $C_{28} \geq 3.99$ (red)] and the solid line marks the 1:1 relation. (bottom) The residuals between these quantities ($\Delta = m_{23.5,i} - m_{tot,i}$) are plotted as a function of i -band surface brightness. Not surprisingly, $m_{23.5,i}$ breaks down as a proxy for total light at $\mu_{e,i} \geq 23.5$ mag arcsec⁻²; our conclusions are not affected by this caveat though.

considered. Interpolated quantities include the surface brightness, ellipticity, and flux enclosed within each elliptical isophote. We then correct for Galactic reddening using the updated version of the Schlegel et al. (1998) prescription by Schlafly & Finkbeiner (2011).

In order to match the resolution of our MLCRs (0.1 mag; Section 3.2), we use only light profiles with $S/N \geq 20$ per isophote, per filter. To meet this requirement, we bin the isophotes for all of the profiles of a given galaxy, marching outwards from the center. The bin sizes are increased until the S/N threshold is met in all bands. This procedure requires as input the S/N as a function of galactocentric radius for each profile. To conform with the adaptive smoothing technique that we apply in our 2D approach (Section 3.3.2), we estimate the S/N of each isophote assuming background-dominated noise. The radius and surface brightness of each bin are computed as weighted averages of the respective input values, where the weights are set to the errors in the original light profiles. Conversely, the enclosed brightness of each bin is simply set to the value for the outermost isophote contained therein. The differential and integrated S/N for each bin are used, respectively, to define the statistical uncertainty in its surface and enclosed brightness. Lastly, the size of the central-most bin for each galaxy is set to match the maximum seeing disk amongst all bands being modelled. This ensures that the colours in these regions are accurately measured. The seeing values for the SHIVir data were taken from McDonald et al. (2011). Note that the binning algorithm employed here is an adaptation of the one described in Roediger et al. (2011a).

For each SHIVir galaxy, the above preparations yield refined luminosity profiles and non-parametric curves of growth for any desired combination of the *grizH* filters. From the former, we measure the necessary colours for each radial bin and compare these data against a set of MLCRs to obtain a profile of M_*/L_i . Combining this profile with its *i*-band curve of growth gives us the cumulative M_* profile and thus the 1D mass within the $R_{23.5,i}$ aperture. At the same time, the integrated colours of the galaxy are extracted from the curves of growth for the same aperture. These colours are then modelled with the same set of MLCRs to arrive at the 0D mass. The major distinction between our 0D and 1D masses is that the latter account for the luminosity and colour gradients in our galaxies, whereas the former simply represent their luminosity-weighted sum.

3.3.2. 2D masses

The starting point of our 2D approach to M_* measurements is the *grizH* imaging for a galaxy. Recall that, while SHIVir’s optical imaging comes entirely from the SDSS, the NIR imaging originate from a number of sources. For the latter, we use preferentially the ULBCam images for several reasons: (i) the field of view ($\sim 8.5' \times 8.5'$) permits Σ_* to be measured to large radii, with good sky sampling; (ii) the photometric depth is high ($\mu_H < 24$ mag arcsec⁻²); (iii) the sensitivity

and spatial distortions have been mapped to high precision; (iv) the sub-sample spans all major galaxy types; (v) the photometric calibration is homogeneous and robust; and, (vi) the small pixel scale ($0.25''$) ensures high spatial resolution for our mass maps. The major disadvantage of the ULBCam imaging is that it lacks an astrometric calibration, which could compromise the accuracy of the measured pixel-by-pixel colours. To overcome this, we computed astrometric solutions⁴ for our optical and NIR images based on the positions of foreground stars. We have used our optical images in this operation for improved homogeneity.

Other steps are required before a galaxy’s colour and stellar mass maps can be computed. The first is to resample the selected images to the largest pixel scale therein (if necessary)⁵. Like Z09, we do not correct the images to a common PSF since this would corrupt their noise properties and thus invalidate our later use of smoothing. Next, we mask foreground stars and background galaxies that fall within the vicinity of the target. While we generally base our masking upon a single image, we make improvements as necessary for light leaked out in other bands. After masking, we place five equal-sized boxes ($N = 100$ pixels) outside the galaxy, in sourceless regions, to measure the background and its variation in each image. The background, which is computed as the mean pixel value amongst the boxes, is subsequently subtracted off. These steps leave us with a set of co-registered, background-subtracted images with uniform resolution.

As in our 1D masses, we prefer that each resolution element included in our 2D masses meet a certain S/N threshold. To this end, we use the technique of adaptive smoothing to boost the S/N of pixels that fall below this threshold. The appeal of this technique is that it preserves the spatial sampling of the original images. However, it comes at the cost of correlating the noise between adjacent pixels in the output. Adaptive spatial binning techniques, such as Voronoi tessellation (Cappellari & Copin 2003), avoid this problem but produces images with irregular renditions of the 2D information. Since these irregularities would complicate our modelling of the pixel-to-pixel colours and extraction of 2D masses (described below), we prefer to raise the S/N of pixels in our images, where necessary, via smoothing.

We smooth our images with the ADAPTSMOOTH code (Zibetti 2009), assuming background-dominated noise. While this assumption ignores the Poisson contribution from the source, the pixels that require smoothing are generally located in regions of low surface brightness, where the background is still dominant (S. Zibetti, *priv. comm.*). Moreover, determining the source’s contribution to the flux in each pixel requires knowledge of the detector gain, which is often poorly

⁴<http://nova.astrometry.net/>

⁵This is done with the SWarp software package – <http://www.astromatic.net/software/swarp>. The output from SWarp has fixed dimensions for each band and is centered on the galaxy, so that adequate sky samples may be later chosen and pixels are properly registered between images.

constrained for stacked images, as in our SHIVir NIR data. We set the noise for each image as the rms variation in the background level and threshold S/N of 20, as per the resolution of our MLCRs. ADAPTSMOOTH is initially run on selected images to obtain a set of smoothing masks that indicate the size of aperture each pixel requires in order to meet the desired S/N threshold in all bands. These masks are then maximally stacked to generate a master mask. We re-run ADAPTSMOOTH on the original images with this master mask in order to apply a consistent smoothing solution to every pixel across all filters. Since smoothing corrupts the noise properties of the output images, we conservatively assume that the S/N in each pixel is the threshold value, thus maximizing the errors. For all ADAPTSMOOTH runs, we limit the smoothing aperture to a radius ≤ 20 pixels. Any pixel requiring a larger aperture in any band is clipped within all output images.

After smoothing, the images are photometrically calibrated at each pixel. Calibration zero-points to the AB magnitude system were kindly provided by M. McDonald. We also correct the images for Galactic extinction, according to Schlafly & Finkbeiner (2011). These final preparations leave us with a set of masked, background-subtracted, and calibrated galaxy images which have a common spatial sampling, registration, and minimum S/N per pixel.

With calibrated surface brightness maps in hand for a select set of filters, we construct the stellar mass map of a galaxy by first computing the minimum number of colours for each pixel (Section 3.2) and transforming those data into a map of M_*/L_i through a set of MLCRs. The mass map follows by simply multiplying the i -band and M_*/L_i maps together. A 2D M_* is then extracted from the mass map by a curve-of-growth analysis. Specifically, we integrate the mass map using a fixed set of elliptical apertures (performed using the XVISTA software package; see Courteau 1996; McDonald et al. 2011; Hall et al. 2012) that match the ellipticity and position angle of the aperture from which the 0D/1D masses were measured. This ensures that extraction methods do not introduce any observed differences between the three versions of our M_* measurements.

4. Results & Discussion

We have described in the previous section our method for modelling the colours of galaxies in terms of their underlying mass-to-light ratio. We can now use this method to quantify the systematics in M_* measurements obtained via MLCRs. While previous studies have addressed various aspects of this topic from a theoretical (idealised) perspective, we use a representative sample of observed local galaxies to focus on the following sources of scatter: (i) SED fitting versus MLCRs; (ii) choice of priors; (iii) choice of constraining data; and (iv) number of spatial dimensions considered. Testing MLCRs with real galaxies should reveal systematics, if any, that are not typically accounted for by the assumed priors. Note that our discussion below is largely based on the BC03 MLCRs.

4.1. The Correspondence Between MLCRs and SED Fitting

In Section 3.1 we used mock galaxies to assess the accuracy of M_* measurements from SED fitting under various conditions of data sampling and quality. Assuming perfect model priors, we found that the scatter in recovered M_* is approximately constant, with ~ 0.1 dex, regardless of the filter combination within the UV-NIR range and whether $S/N = 10$ or 20 is achieved (see Fig. 1)⁶. Since SED-based M_*/L measurements should be less biased than those from MLCRs (T11), by design, this result provides us with a useful benchmark for evaluating the quality of MLCR-based results, which is the aim of this section.

We take two complementary approaches to test the correspondence between SED fitting and MLCRs, both of which focus on the recovery of M_* . The first approach uses mock galaxies. The advantages of this approach are that: (i) the mass to be recovered is known in each case, and (ii) randomly-drawn mock galaxies should populate a significant fraction of the observational space spanned by a given MLCR set. Therefore, mock galaxies offer a most direct way to uncover any biases introduced by MLCRs.

For our mock galaxy sample, we draw 500 stellar SEDs from the MAGPHYS/BC03 library. In Figure 5 we assess the accuracies of the MLCR-based masses and trends therein with galaxy parameters under the same scenarios of data breadth and quality as assumed for the green and orange points in Fig. 1 (i.e. *grizH* and *gi* band combinations, $S/N = 20$). For simplicity, we use the same layout and colour scheme as before.

Fig. 5 shows that our MLCR method yields residual distributions that closely resemble those seen in Fig. 1 and, as before, we see hints of trends in the residuals as a function of metallicity and t_{burst} . Moreover, the residuals from our method have nearly identical properties to those that were found for SED fitting, with a mean value of (essentially) zero and dispersion of 0.13-0.14 dex. Similar results are obtained when other combinations of the SHIVir bands are used (i.e. *giH* and *griH*). This complements the work of GB09, who found that M_*/L could be satisfactorily recovered for mock galaxies using the $g-i$ colour, except those characterized by intermediate-age populations and bursty SFHs (where M_*/L was biased to higher values by 0.15 dex, in the median). For galaxies well-described by the MAGPHYS priors then, we infer that there is essentially no difference between the masses measured via SED fitting or MLCRs. Furthermore, Fig. 5 indicates that minimal observational constraints are needed to achieve an accuracy of 33% in the M_* measurements for such galaxies.

The correspondence between SED fitting and MLCRs for mock galaxies was to be expected

⁶In particular, M_* measured from SEDs sampled with only the *gi* filters fare equally well as those determined using filters throughout the UV-NIR wavelength range.

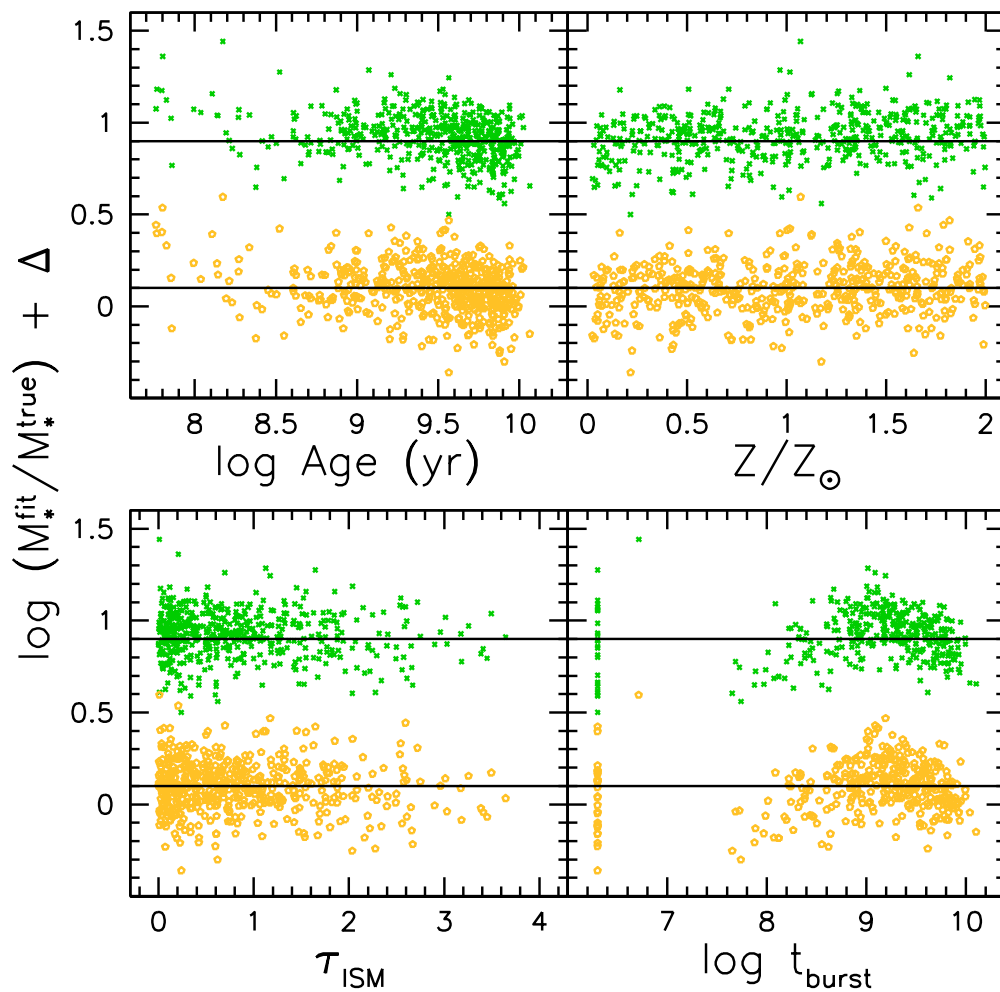


Fig. 5.— As in Fig. 1 but for M_* measured via MLCRs (rather than SED fitting) and SEDs sampled with the *grizH* (green) and *gi* (orange) filters, and $S/N = 20$. In both cases we find that the residuals have a distribution with zero mean and 0.13-0.14 dex of dispersion. Similar results are found for the *giH* and *griH* filter combinations.

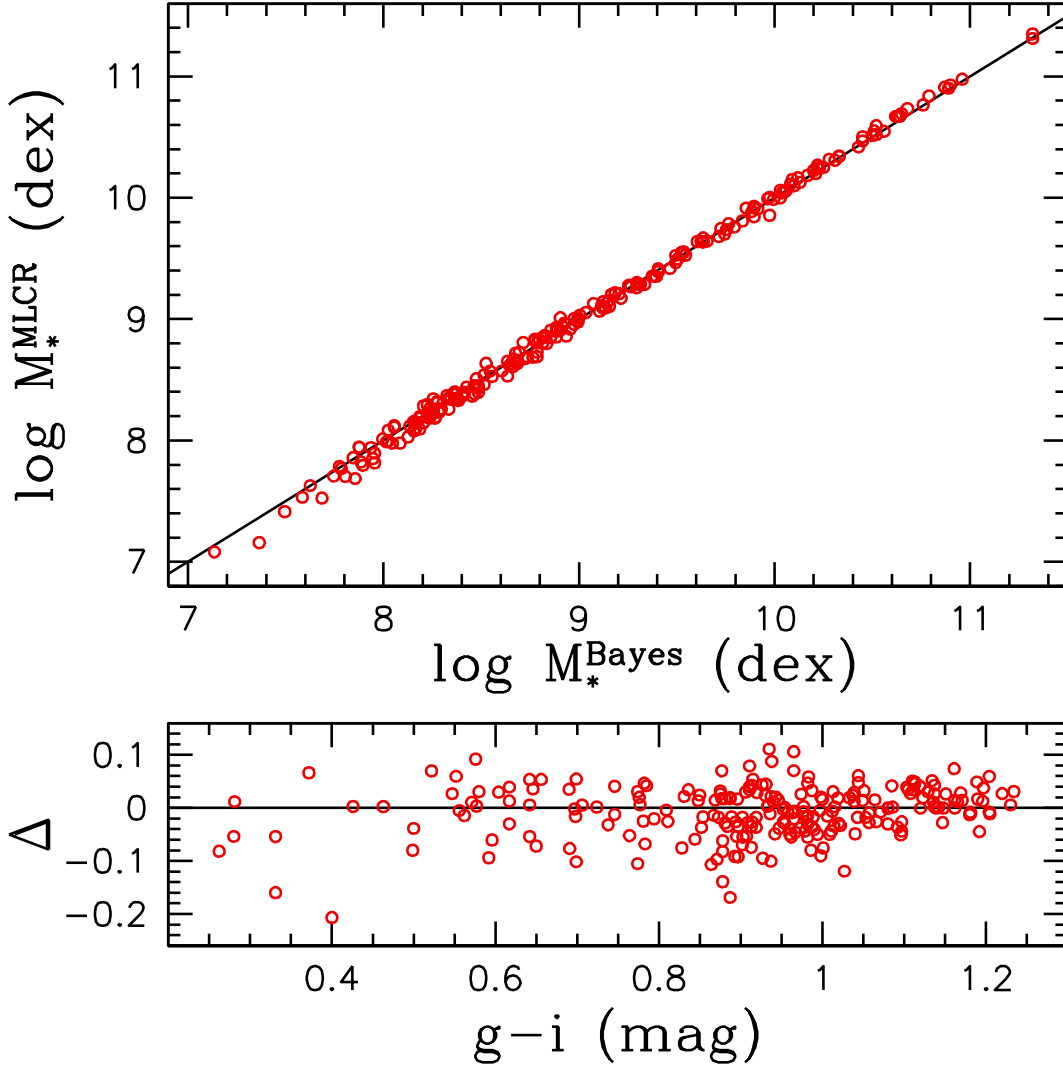


Fig. 6.— (top) M_* estimates from our multi-MLCR method (M_*^{MLCR}) versus those from Bayesian SED modeling (M_*^{Bayes}). Both sets of masses are derived using the MAGPHYS/BC03 library and the integrated *grizH* SEDs of SHIVir galaxies. (bottom) Residuals, computed as $\Delta = \log M_*^{\text{MLCR}} - \log M_*^{\text{Bayes}}$, are plotted as a function of $g-i$ colour. The correspondence between the two techniques is clearly excellent over the full range of colours probed by our dataset ($\bar{\Delta} = -0.01$ dex; $\sigma = 0.05$ dex).

since we drew their SEDs from the same SPS model library that was used to build our MLCRs. Our second approach to testing this correspondence overcomes this bias by working with real galaxies. In all likelihood, real galaxies populate M_*/L -colour space differently than our synthetic models, in which case the two methods should yield discrepant results, as demonstrated in T11. A corollary to this is that a sample of real galaxies may not span the same range of colours as our models, in which case our second approach can only inform us of the correspondence between SED fitting and MLCRs over a limited interval. SHIVir galaxies, for instance, may be biased to redder colours since they inhabit a cluster environment. Still, the outcome of this second approach complements the previous one and will provide some context to forthcoming tests.

Figure 6 compares M_* for SHIVir galaxies obtained from MLCRs and SED fitting. Note that this comparison assumes that SED fitting yields the most accurate masses for real galaxies. Both sets of M_* were determined from the integrated $grizH$ SEDs of these galaxies – the results for cases involving other bandpass combinations are rather similar. The top panel of Fig. 6 indicates that the two methods are in excellent agreement, with a mean residual of -0.01 dex and 0.05 dex of dispersion, while the lower panel shows that the residuals are independent of galaxy colour, although the sampling for $g-i < 0.6$ is admittedly poor. This is at odds with T11, who emphasised the bias imparted by MLCRs on M_* , but our use of multiple colours explains this difference. For instance, if we used the $g-i$ colour only, we would tend to overestimate M_*/L_i , in agreement with T11 (see Fig. 10).

The above tests demonstrate the two following points about our multi-MLCR method: (i) like SED fitting, it recovers the known M_* of mock galaxies to better than ± 0.15 dex; and (ii) it reproduces M_* from SED fitting to real galaxies to within ± 0.05 dex. The increased accuracy in the latter case is likely caused by the smaller colour range spanned by the SHIVir galaxies, compared to our mock dataset. These findings indicate that our multi-MLCR method may be counted on to yield fairly accurate results.

4.2. The Underlying Priors of MLCRs

We have shown in the previous section that MLCRs produce, on average, equivalent results to SED fitting. However, this does not entail that MLCRs and how they are used are completely free of systematics. Since an MLCR set is constructed from an SPS model library, the priors underlying the model ingredients or how the models are implemented can contribute significantly to the error budget. Specifically, any SPS model library parameter that affects the relationships between colour, age, metallicity, reddening, and M_*/L will govern our results. For instance, omitting a burst component from model SFHs will bias M_*/L to higher values. Given the well-studied role that model priors play in SED-based M_* (Conroy 2013; Courteau et al. 2014), we now examine

how these effects are manifested in MLCR-based M_* . We omit the choice of IMF from the following since its effect, while significant ($\Delta M_* \sim 0.3$ dex), is well understood in most cases (e.g. van Dokkum 2008; Longhetti & Saracco 2009; Courteau et al. 2014).

A straightforward approach to assess the effect that priors have on MLCR-based M_* is to compare MLCRs calibrated with different model libraries. This is achieved in Figures 7-8, where the MLCRs are either of our own creation or drawn from the literature. These plots are structured similarly to Fig. 2 though the first focusses on optical colours accessible through SHIVir and the second on optical-NIR colours. Our own MLCRs correspond to calibrations based on the BC03 and CB07 versions of the MAGPHYS library, as well as the SPS model of Conroy et al. (2009, hereafter FSPS). FSPS provides the proper machinery to create libraries like MAGPHYS. With it, we have computed 50,000 SEDs which adhere as closely possible to the MAGPHYS priors. Adhering to these priors allows us to gauge the impact that the choice of SPS model has on MLCRs. Two exceptions to our adherence include the shape of the effective absorption curve for birth cloud dust and the treatment of bursts of star formation. In MAGPHYS, the optical depths of ambient and birth cloud dust are parameterized as power laws in wavelength to different exponents (-0.7 and -1.3, respectively), while bursts occur randomly throughout each model’s lifetime and can last anywhere from 0.03-0.3 Gyr. In FSPS, both dust components are simultaneously described by a single power-law relation, albeit with an adjustable exponent, while only one instantaneous burst can be added to any model’s SFH. For those readers interested in incorporating our BC03 and FSPS MLCRs into their own work, we present tabulations of linear least-squares fits to these relations in the Appendix.

For the literature MLCRs in Fig. 7, we show the calibrations of B03, Z09, T11, and IP13. We omit the MLCR sets of Bdj01 and MS14 given their Johnson-Cousins band calibrations, whereas our focus is on the SDSS + 2MASS suite. GB09 did not tabulate the MLCRs used in their work but we suspect that they are well-matched to those of Z09. The number of literature MLCRs shown in Fig. 7 depends on the colours examined here. For instance, the T11 MLCR was only defined in terms of $g-i$. Whenever possible, we have restricted the range of colours spanned by the literature MLCRs to those advocated by their respective authors. This is why, for example, the T11 and IP13 MLCRs do not span the full baselines of the panels in which they appear. An important distinction about the trends shown in Fig. 7 is that those from B03 and T11 were constrained by their authors using SED fits to real galaxies, while all others are purely theoretical. Lastly, the B03 relations have been reduced by 0.15 dex to correct their choice of a “diet-Salpeter IMF” to a Chabrier (2003) IMF.

In Fig. 2 we demonstrated that, in the case of our BC03 MLCRs, M_*/L_i follows a largely monotonic relationship with each one of the colours defined by the *grizH* bands. Figs. 7-8 show that this behaviour is likewise reflected, albeit to different degrees, by other sets of MLCRs. The

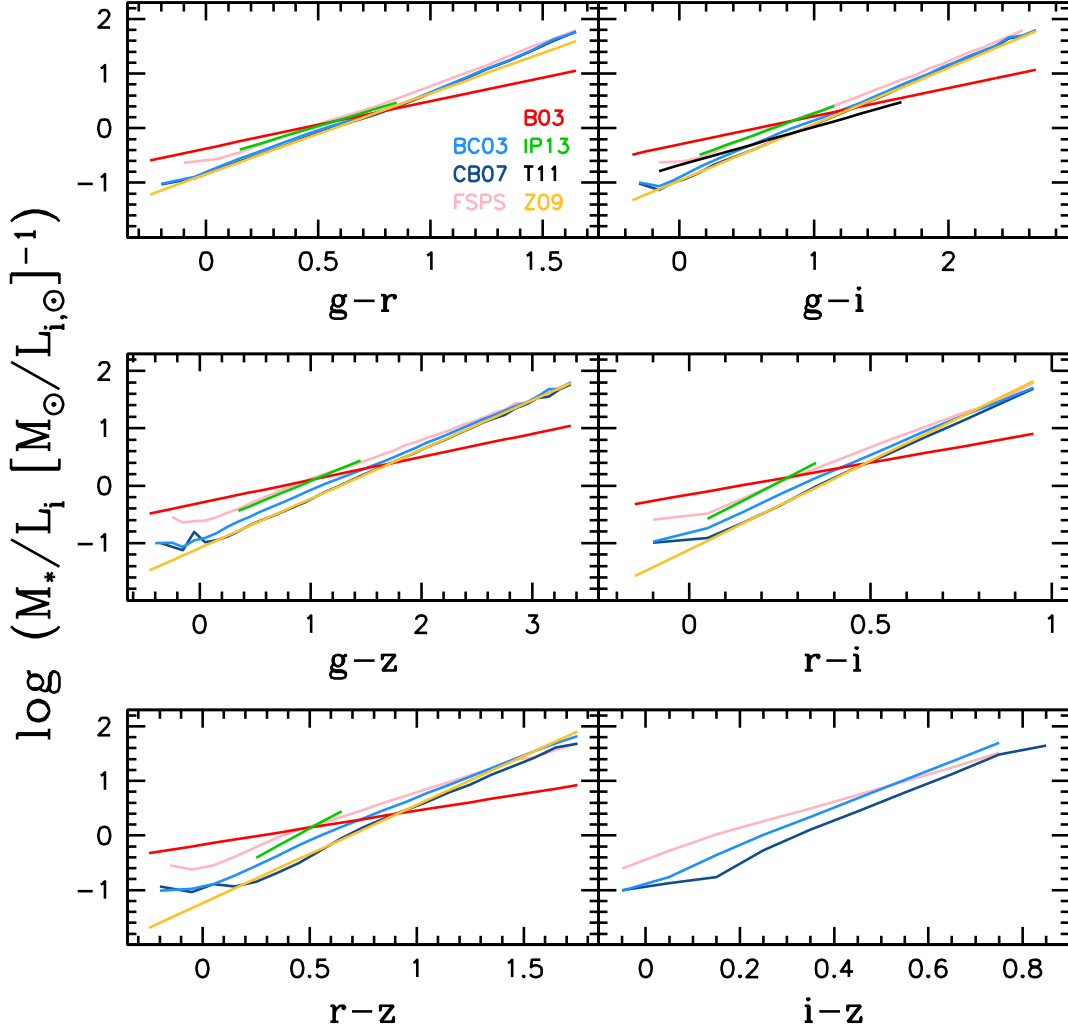


Fig. 7.— As in Fig. 2 but now showing the MLCRs predicted for SHIVir optical colours from libraries of different SPS models (BC03; CB07; Conroy et al. 2009, hereafter FSPS) or related work in the literature (Bell et al. 2003, Zibetti et al. 2009, Taylor et al. 2011, Into & Portinari 2013; hereafter B03, Z09, T11, and IP13, respectively). Note that the B03 and T11 MLCRs are constrained empirically by SED fits to real galaxies while all others are fully theoretical – the BC03, CB07, and FSPS relations are of our own making. Also, the B03 relations have been reduced by 0.15 dex to change the underlying initial mass function (IMF) to the Kroupa/Chabrier form used by all other MLCRs shown here and the IP13 relations correspond to their exponential star formation history model.

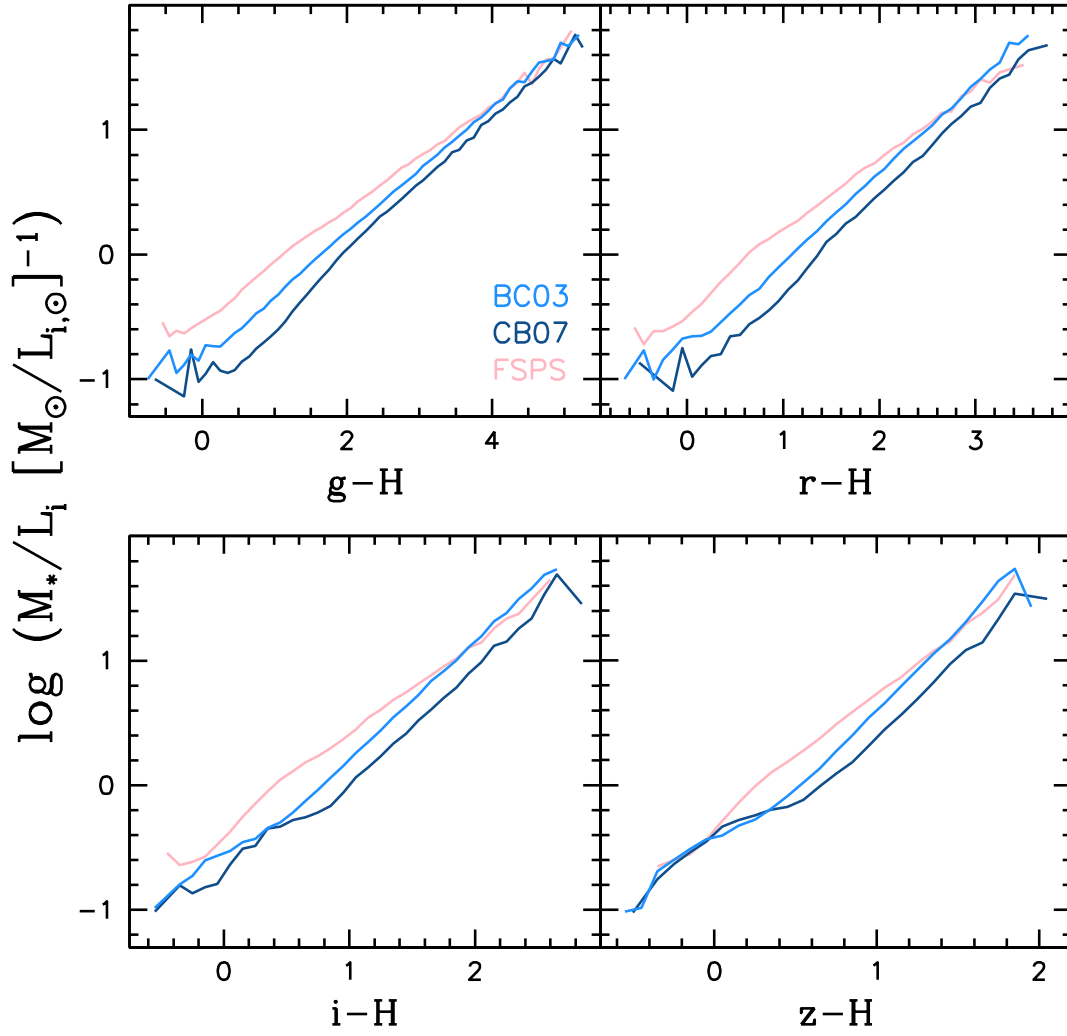


Fig. 8.— As in Fig. 7 but now comparing MLCRs predicted for SHIVir optical-NIR colours, where available.

reason for this is simple: as the age, metallicity, and/or reddening of a stellar population increases, so do its M_*/L and colours.

Fig. 7 highlights that the best agreement between the optical MLCRs occurs with $g-r$ and $g-i$, while all other colours are characterized by notable discrepancies. Not surprisingly, the CB07 and Z09 MLCRs compare very well in all panels since they were both derived from the MAGPHYS/CB07 library. B03 notwithstanding, these two calibrations also predict the lowest M_*/L_i values for any colour; we therefore focus the following comparisons around the CB07 MLCRs. All other MLCRs, except those of B03 and T11, usually agree better with the CB07 calibration towards redder colours (i.e. older, more metal-rich, and/or highly-reddened populations), but the improvement for IP13 is admittedly marginal. Towards bluer colours (i.e. younger, more metal-poor, and/or dust-free populations), these same MLCRs can differ from the CB07 calibration by as much as ~ 0.3 dex. The FSPS MLCR, on the other hand, predicts a higher M_*/L_i by 0.5 dex for the bluest colours. The absolute discrepancy between the T11 and CB07 MLCRs falls within the range < 0.3 dex at all colours.

The above observations from Fig. 7 indicate that the systematic error in MLCR-based M_*/L varies as a function of colour. The cause of this colour-dependent error must be due, in part, to the different physics encoded by their underlying priors. It is noteworthy that the B03 and T11 MLCRs possess the shallowest slopes, since these are the only relations shown in Fig. 7 that were calibrated using real galaxies. To what extent this difference reflects a genuine flaw in theoretical MLCRs is unclear given the marked differences in the priors between them and the empirically-constrained MLCRs. For instance, T11 did not include bursts in their model SFHs and B03 limited the strength of such events to $\leq 10\%$ by mass, whereas the MAGPHYS library incorporates a variety of bursty SFHs. Furthermore, B03 omitted reddening from their models, while T11 and MAGPHYS invoked the Calzetti et al. (2000) and Charlot & Fall (2000) extinction laws, respectively. Teasing out the relative contributions of priors and the real galaxy distribution in the M_*/L -colour plane to the slopes of the B03 and T11 MLCRs is non-trivial and lies beyond the scope of this work. Furthermore, this comparison between empirical and theoretical MLCRs can only inform us on the systematics of modelling integrated light. Investigations like B03 and T11, though based on spatially-resolved data, have yet to be performed.

Turning to Fig. 8, we find that the systematic errors incurred by using optical-NIR colours are often much worse than those associated with optical colours alone. This contradicts the popular belief that NIR data yield the most accurate M_*/L measurements. We confirm Z09's claim that the optical-NIR MLCRs for the MAGPHYS/BC03 library tend to exceed those of the MAGPHYS/CB07 library, often by as much as 0.3 dex. Since the main change to the CB07 model was to increase the NIR flux of TP-AGB stars (Bruzual 2007), we attribute this difference to the role of this stage of stellar evolution to the error budget. Supporting this interpretation is the fact that these

SPS models are implemented identically in the MAGPHYS library, and therefore any differences between their MLCRs must be rooted in their most basic ingredients.

Although significant, the differences between the BC03 and CB07 optical-NIR MLCRs pale in comparison to those between the CB07 and FSPS MLCRs, which can exceed 0.6 dex. To help identify the source of this discrepancy, we show in Figure 9 the MLCRs corresponding to the simple stellar populations (SSPs) of the BC03, CB07, and FSPS models, at solar metallicity. Since the CB07 and FSPS models incorporate the same isochrones (Marigo & Girardi 2007; Marigo et al. 2008), we expect that the MLCRs for their SSPs should follow each other. Instead, the CB07/SSP MLCRs abruptly diverge from the FSPS/SSP MLCRs to redder optical-NIR colours at an age of ~ 0.1 Gyr, and remain well-separated for another ~ 1.5 -1.6 Gyr. During that time period, the FSPS/SSP MLCRs actually follow the BC03/SSP relations. These behaviours qualitatively persist at lower metallicities as well (e.g. $Z = 0.004$). The above age range is well-known as the period in which TP-AGB stars are present in SSPs. Therefore, the TP-AGB treatment must be contributing to the observed differences between the CB07 and FSPS optical-NIR MLCRs too. However, Fig. 8 shows that the FSPS MLCRs also lie above the BC03 MLCRs, despite the similar trends exhibited by their SSPs in Fig. 9. We suggest then that the much burstier nature of the MAGPHYS SFHs helps drive the differences between the FSPS and BC03/CB07 MLCRs as well. The flat prior on the burst mass fraction in MAGPHYS and the fact that half of its SFHs incorporate a recent burst suggest that our BC03/CB07 MLCRs are biased to stellar populations with younger mass-weighted ages than our FSPS MLCRs. Our suggestion is consistent with the rank order of these MLCRs in Figs. 7-8, in which the BC03/CB07 MLCRs predict a lower M_*/L_i at bluer colours than do the FSPS MLCRs. Caution must therefore be taken when interpreting M_* measurements that are based on optical-NIR MLCRs.

4.3. The Impact of SED Sampling

Figs. 7-8 highlighted the systematic penalty incurred with the MLCR method through the choice of an SPS model library. Particularly striking was the inflated disagreement between MLCR sets when optical-NIR colours are included. However, it is conceivable that, within the context of a single MLCR set, the M_*/L measured for a galaxy would also vary as a function of the data considered. One reason could be the fact that not all colours are equally sensitive to the parameters that establish M_*/L , such that the use of multiple colours might enhance one’s constraining power. Another could be that the fluxes predicted by SPS models within one or more filters are inaccurate, which likewise would affect all colours associated therewith. Given these concerns, we address in this section whether or not the degree of SED sampling contributes meaningfully to the systematics of MLCRs.

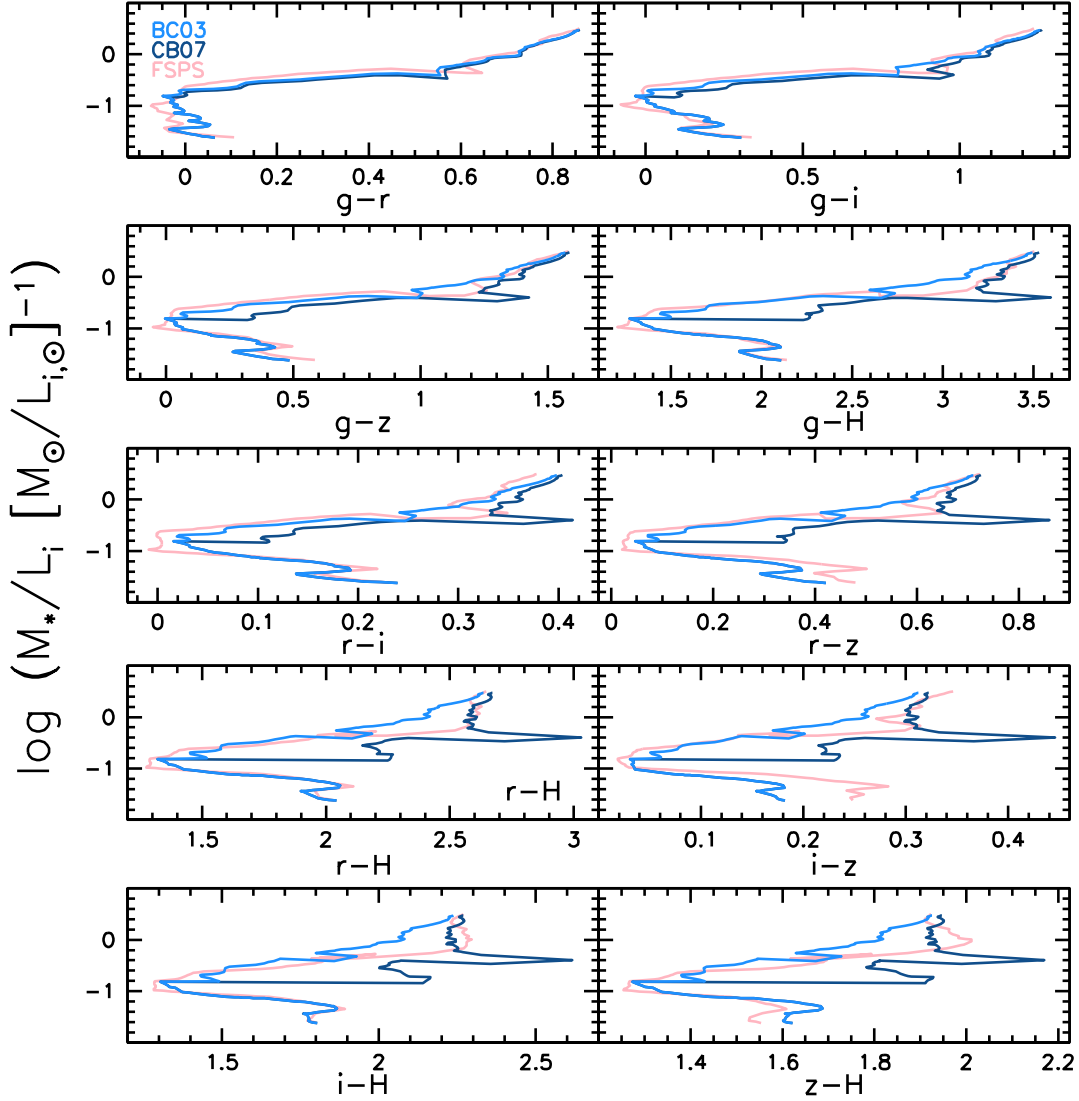


Fig. 9.— As in Fig. 7 but now comparing the MLCRs based on SSPs of solar metallicity drawn from the BC03, CB07, and FSPS SPS models, and for all SHIVir colours simultaneously. Similar trends are also found amongst these SSPs at lower metallicities (e.g. $Z = 0.004$).

To assess the impact of SED sampling, we shall test the robustness of our multi-MLCR method under a variety of realizations of the SHIVir data. We compare in Figure 10 sets of M_* measured for these galaxies via our BC03 MLCRs and SEDs sampled with the following filter combinations: gi , giH , $griH$, and $grizH$. The layout of this figure is identical to Fig. 6) and we use the same combinations of colours as before in the fits for each SED realization. The gi -, giH -, and $griH$ -based M_* are plotted in the top panel as a function of the $grizH$ -based M_* , which we take to be the most accurate (see Fig. 6). In the bottom panel we plot the residuals between the former and latter as a function of the $g-i$ colour.

Fig. 10 demonstrates that the $grizH$ -based masses of SHIVir galaxies are reproduced well by those using the $griH$ and giH band combinations instead. The gi -based values, on the other hand, are biased to slightly higher values, by 12% on average, implying that the $g-i$ colour systematically overestimates M_*/L_i , in agreement with the findings of T11. In the bottom panel, we see that the residuals from the various realizations of the SHIVir dataset are robust to galaxy colour but, as in Fig. 6, this conclusion is tentative for systems with the bluest colours ($g-i < 0.6$).

The robustness of M_* for SHIVir galaxies is explained by how we combine M_*/L_i values when multiple colours are fitted. Recall that we construct a master M_*/L_i for each object by computing a weighted mean of the values that were assigned to its colours. Our method then naturally assigns greater weight to those colours which have less scatter in their MLCRs. In the case of Fig. 10, the colour that maintains the robustness amongst the various sets of M_* is $g-i$. Indeed, Fig. 2 demonstrates (via the dashed lines) how the scatter in M_*/L_i is minimized for the $g-i$ MLCR, relative to the $g-r$, $g-z$, and $g-H$ MLCRs.

Since most sets of M_* presented in Fig. 10 are mutually consistent, one may be tempted to conclude that the r and z bands do not increase the constraining power of our method. While it is true that including these bands does not change M_*/L_i significantly, a positive statistical impact is made on the assigned errors. The mean error on M_*/L_i with the gi , giH , $griH$, and $grizH$ SEDs of SHIVir galaxies, is 0.29, 0.22, 0.18, and 0.15 dex, respectively. Thus while the $g-i$ colour may be counted on to reasonably determine M_* when other photometry is scarce and/or unreliable, the desirable combination of high accuracy and precision is achieved by applying MLCRs to well-sampled SEDs.

4.4. Must Mass Estimates be Spatially-Resolved?

We now examine the claim that M_* is more accurately measured on the basis of spatially-resolved data than integrated fluxes (Z09). According to this claim, the method by which one measures a galaxy M_* is most relevant if a significant amount of it (e.g. >10%) is hidden by

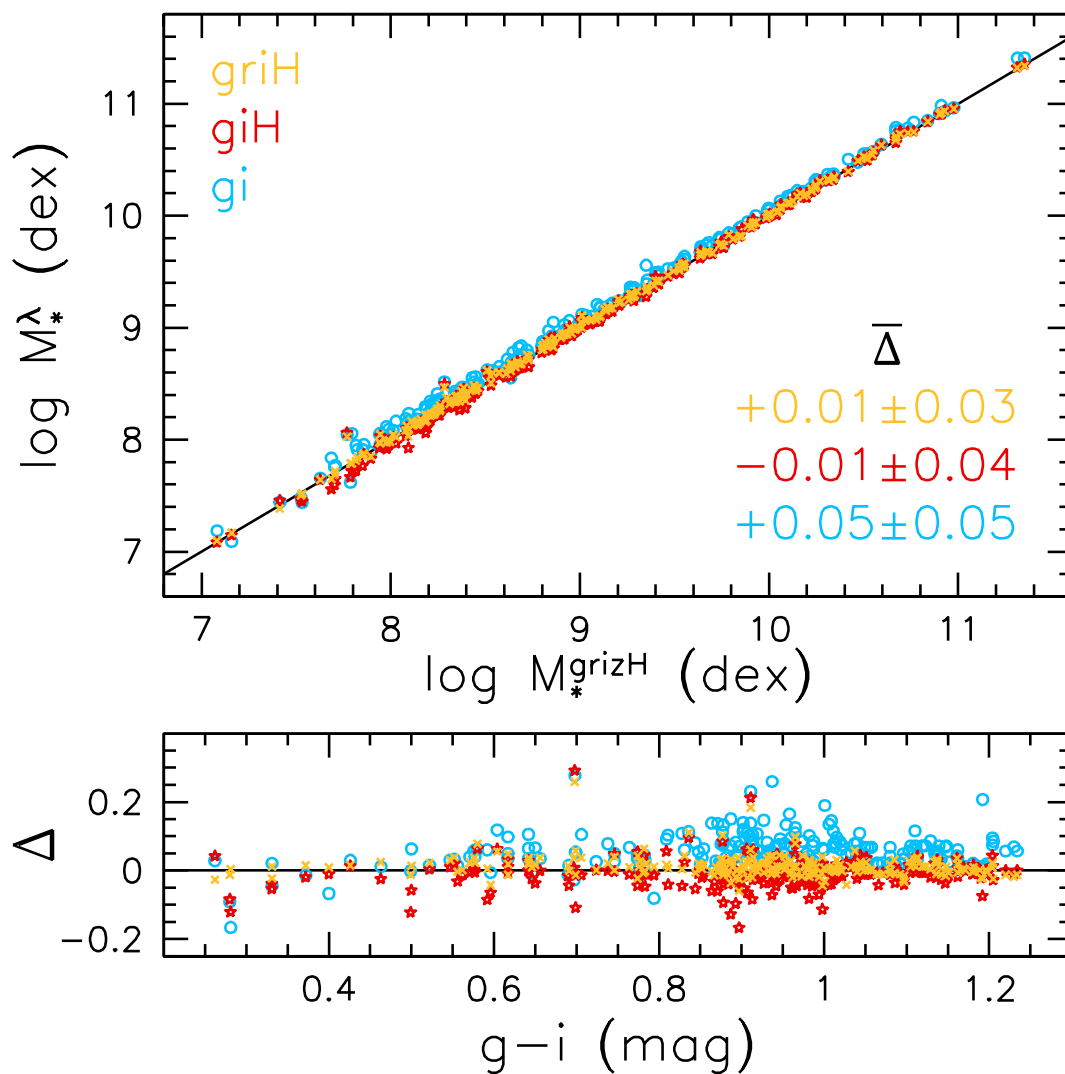


Fig. 10.— (top) Comparison of M_* estimates from our multi-MLCR method for various realizations of the SHIVir dataset. Masses derived from the filter combinations gi , giH and $griH$ are plotted against those measured from the $grizH$ bands. (bottom) Residuals, computed as $\Delta = \log M_*^\lambda - \log M_*^{\text{grizH}}$, are plotted as a function of $g-i$ colour. The mean and dispersion of each residual distribution are quoted in the top panel. These values indicate that our method is modestly robust to SED sampling.

bright stars and/or dust. Higher-dimensional approaches to measuring M_* presumably overcome this bias by assigning each galaxy resolution element a M_*/L tailored to its colours. In other words, allowing M_*/L to vary spatially within a galaxy may be essential to ensure an accurate determination of its M_* .

The need for a 2D approach to measuring M_* was first demonstrated by Z09. Using optical and NIR imaging, they found that the M_*^{0D} of spiral galaxies could be lower than their M_*^{2D} by as much as 0.15 dex. Conversely, the 2D approach produced hardly any change in M_* for the lone early-type galaxy in their sample. The authors thus claimed that the discrepancy between M_*^{0D} and M_*^{2D} increases towards later galaxy types. The Z09 sample, however, was small and biased to late-type spirals. We have improved upon this limitation by expanding the work of Z09 to a larger, more representative set of local (SHIVir) galaxies (see also SS15). Similarly, the use of a 1D approach (via luminosity profiles) may also yield improved M_* measurements, by accounting for the colour gradients which many galaxies are known to possess Roediger et al. (2011a). A 1D approach is also more straightforward and less computationally-expensive than its 2D cousin. We therefore explore the relation between M_*^{0D} and M_*^{1D} in this section as well.

Figure 11 compares the 0D and 1D M_* for SHIVir galaxies based on SEDs sampled with either the gi , giH , $griH$, or $grizH$ bands. The correspondence between the 0D and 1D values is clearly excellent in most cases, in the sense that there is no net bias, as evidenced by the residual statistics. The major outliers are understood as being due to cases of extreme colour gradients, where a positive gradient would lead to $M_*^{1D} > M_*^{0D}$ and vice versa. Omitting the outliers, we infer that radial variations of M_*/L_i within galaxies, on average, bias 0D measurements by no more than $\pm 20\%$. Several explanations could apply here: (i) most galaxies have mild colour gradients; (ii) as in (i) but only for those colours which possess steep MLCRs (e.g. $g-r$), or (iii) M_*/L_i variations occur in regions of galaxies which do not enclose large fractions of their total light. We propose that the third explanation applies most often, as earlier work by our group (Roediger et al. 2011a) demonstrated that significant colour gradients are commonly found within the SHIVir sample.

Fig. 11 suggests that colour gradients do not affect M_* measurements for our galaxies to a large degree. In addition to the radial coordinate though, galaxy colours can vary with azimuth and asymmetrically (i.e. pixel-by-pixel). 1D masses are exempt from these other possible dependencies by virtue of the isophotal fitting that is used to measure luminosity profiles of galaxies. 2D masses, however, are sensitive to all three. To address the significance of the latter two dependencies, and the veracity of Z09’s conclusions, we have derived 2D masses for 18 nearly face-on SHIVir galaxies, which is twice the size of Z09’s sample⁷ Some basic properties of our 2D sub-sample are

⁷Computational constraints limited us to this sub-sample. We will present the mass maps for all the ~ 280 SHIVir galaxies in a forthcoming publication. SS15 have also recently computed 2D masses for 67 nearby galaxies.

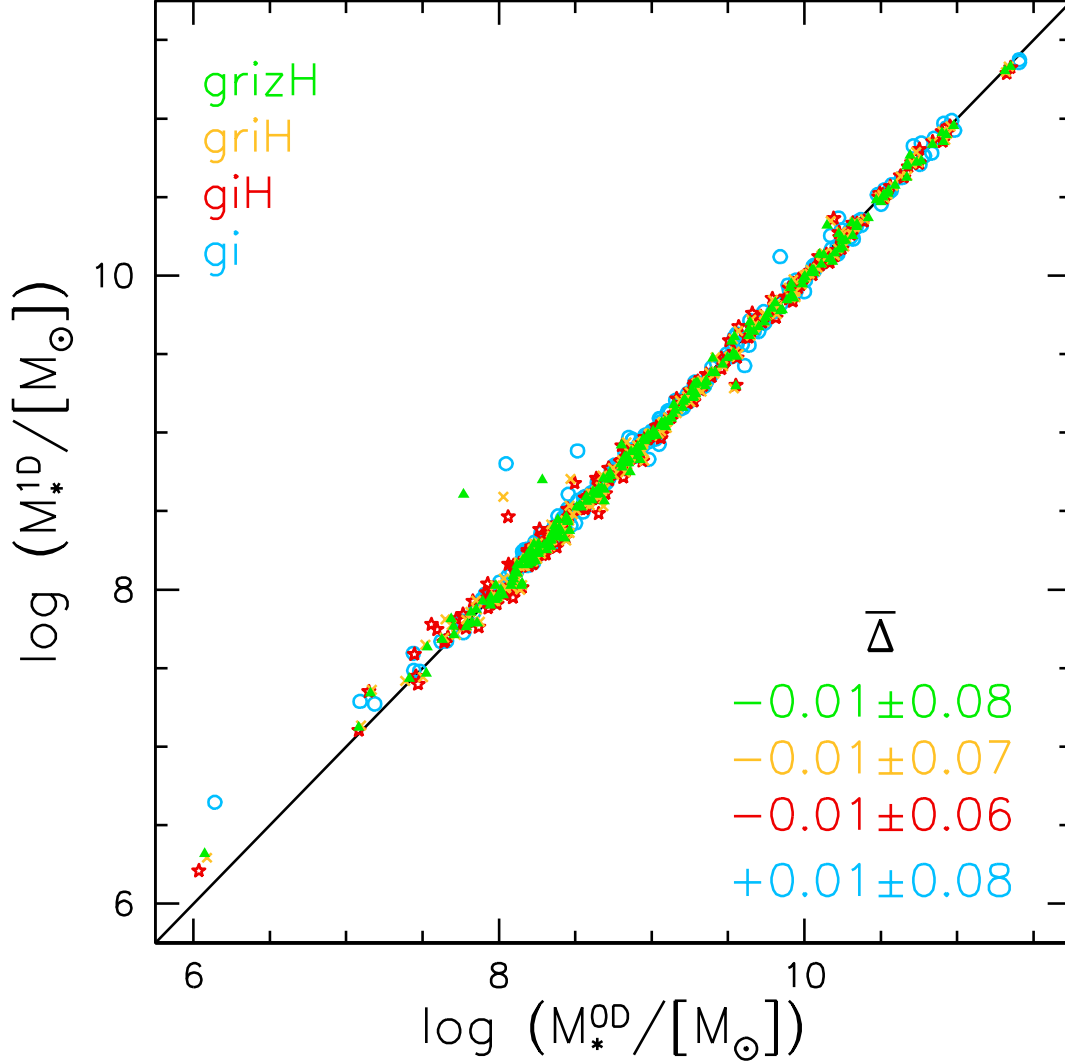


Fig. 11.— M_* estimates from the integration of stellar mass density profiles (M_*^{1D}) versus those from integrated photometry (M_*^{0D}). Both sets of masses have been derived for various realizations of the SHIVir dataset (*gi*; *giH*; *griH*; *grizH*). The mean residuals and dispersions (tabulated at lower-right) suggest that, for our sample, colour gradients do not introduce a persistent, significant bias in M_*^{0D} .

listed in Table 1. The morphological distribution (column 5) show that this sub-sample represents the present-day galaxy population quite well, spanning the giant early-types, spirals, and both flavours of dwarves (gas-rich and -poor). Their 0D M_* should thus encompass the full range of biases mentioned above, if indeed present.

The 0D and 2D galaxy M_* are compared in Figure 12. As for Fig. 11, we have measured 2D M_* (see Table 1) for a variety of colour combinations, which amounts to iteratively dropping filters from the full SHIVir suite (*grizH*). Unlike our 0D-1D comparison, we plot the ratio $\log(M_*^{2D}/M_*^{0D})$ instead, where galaxies with $M_*^{2D} > M_*^{0D}$ lie above the horizontal line that marks equality. Plotting this ratio allows us to order galaxies from early-types on the left to late-types on the right, and thus to gauge the existence of any correlations with morphology. Note that each vertical cluster of blue, green, orange, and red points represents a single galaxy and the dwarf galaxies in our 2D sub-sample appear as the four leftmost members of the early-type group and the four members of the "Im/BCD" group. Arrows represent cases where only lower limits could be placed on the 2D masses, while hollow points denote cases in which 0D masses are unreliable. The former occur when *ADAPTSMOOTH* cannot build enough S/N out to $R_{23,5,i}$ and the latter when one or more colours exceed the ranges of our MLCRs. The error bars shown in the lower-right corner represent the average uncertainty in the 0D masses for these galaxies, and should thus be regarded as lower limits.

Fig. 12 shows that our 2D approach produces mixed results with respect to 0D values, depending on the data involved. M_*^{2D} most often exceeds M_*^{0D} when the SEDs of pixels are sampled with the *gi* band combination. In the median however, this excess is quite small for early-types (dwarves + giants; 0.02 dex) and zero for spirals, the reason being that many members of these groups lie about the $M_*^{2D} = M_*^{0D}$ line. While late-type dwarfs possess amongst the highest values of $\log(M_*^{2D}/M_*^{0D})$ when the *gi* bands are used, the small size of their group prevents us from drawing firm conclusions. Nevertheless, the offsets seen for some of our Im/BCD's agrees with the fact that these galaxies often host pockets of recent star formation, which would far outshine their underlying (low surface brightness) stellar disks/spheroids. In other words, we expect the integrated light of these galaxies to be biased blue and, accordingly, low M_*/L .

Although the offsets between M_*^{0D} and M_*^{2D} are *typically* small for most galaxy types when using only the *gi* bands, they can be most significant on a case-by-case basis. For instance, VCC 1437, an elliptical galaxy with a very blue center (most likely due to recent star formation), has $M_*^{2D} > M_*^{0D}$ by 0.15 dex, while three of the Im/BCD galaxies in our 2D sub-sample have absolute $\log(M_*^{2D}/M_*^{0D})$ values of >0.1 dex. Our foremost conclusion regarding M_*^{0D} measurements based on optical information alone is that internal variations in M_*/L may be captured by including an additional random component in the error budget for all populations. Our best estimate of the size of this component is 0.05 dex for early-types and 0.03 dex for spirals; these values can be refined

Table 1. Bulk properties of Virgo cluster galaxy sub-sample used for 2D mass map experiment¹

NGC ID (1)	VCC ID (2)	α_{2000} (deg) (3)	δ_{2000} (deg) (4)	Type ² (5)	M^3 (mag) (6)	C_{28} (7)	μ_e (mag arcsec ⁻²) (8)	R_e^3 (kpc) (9)
–	0389	185.0138	14.9614	dS0	-18.32	3.690	22.16	1.454
–	0751	186.2012	18.1950	dS0	-17.68	3.374	22.00	0.994
–	0788	186.3200	11.6053	dE	-15.98	2.992	23.26	0.970
–	0816	186.4000	15.8478	dE	-17.70	2.665	24.46	3.210
–	1437	188.1396	9.1736	E	-16.96	4.055	21.00	0.437
–	1440	188.1392	15.4153	E	-17.87	5.797	22.12	0.914
4503	1412	188.0258	11.1764	S0	-20.76	4.701	20.83	2.308
–	1358	187.8467	17.2064	Sa	-16.91	2.679	23.23	1.361
4584	1757	189.5746	13.1100	Sa	-18.65	3.464	22.05	1.744
4407	0912	186.6342	12.6111	Sab	-19.64	3.411	22.07	2.919
4394	0857	186.4812	18.2142	Sb	-21.03	4.239	22.01	4.284
–	2023	191.3833	13.3325	Sc	-17.80	1.943	23.33	2.377
–	0510	185.4738	15.6458	Sd	-17.42	3.391	23.55	1.916
4519	1508	188.3758	8.6547	Sd	-19.50	2.897	22.12	2.775
–	0583	185.6875	15.5022	Im	-16.83	2.384	24.04	1.758
–	0980	186.7967	15.8967	Im	-17.52	2.488	23.60	2.373
–	1725	189.4229	8.5586	BCD	-17.23	2.052	23.30	1.777
–	1804	189.9171	9.3989	BCD	-16.35	3.427	23.70	1.324

¹The parameters M , C_{28} , μ_e , and R_e correspond to i -band values.

²Drawn from the NASA Extragalactic Database.

³Estimated assuming a common distance to all Virgo cluster galaxies of 16.5 Mpc (i.e. $m-M = 31.087$ mag; Mei et al. 2007).

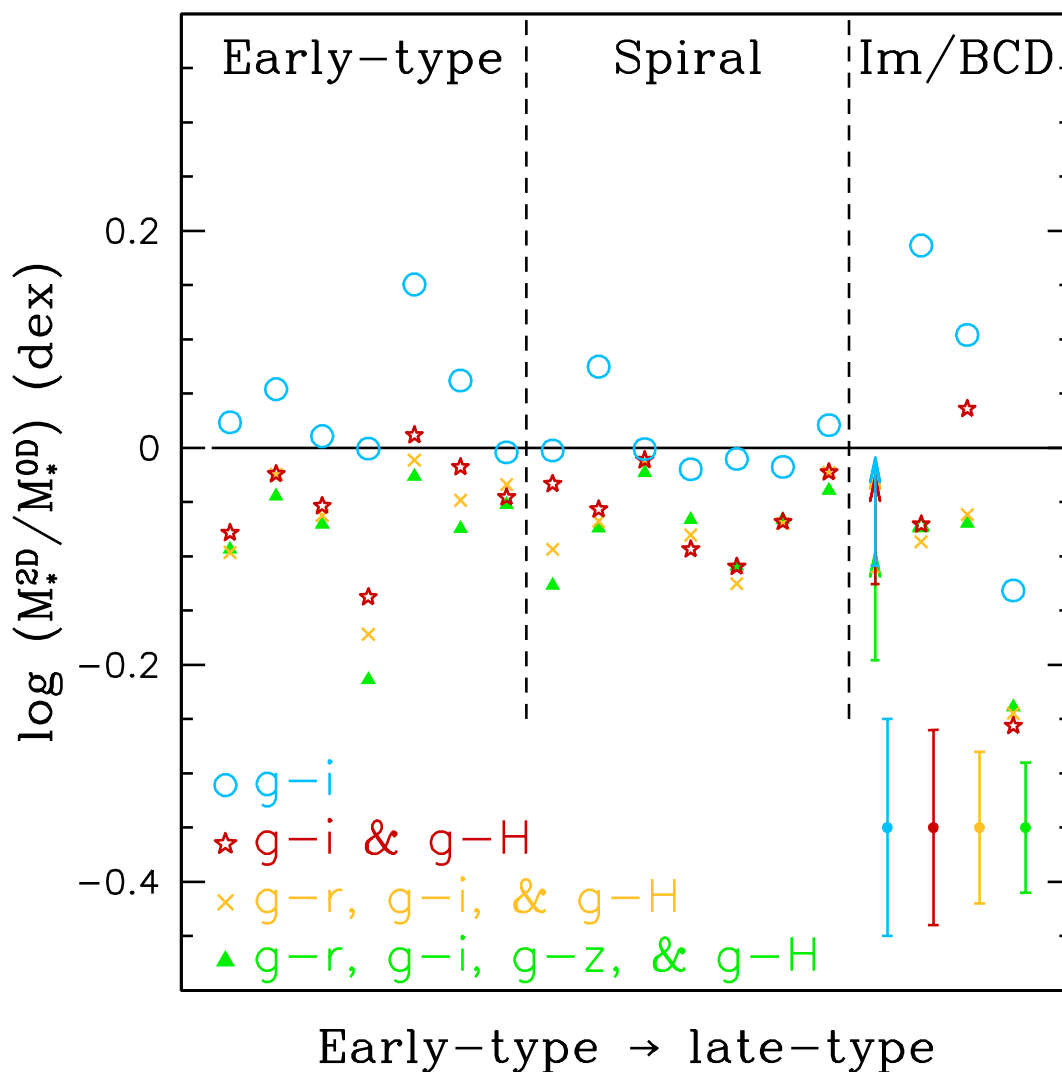


Fig. 12.— Comparison of M_* values derived from integrating the Σ_* maps for 18 SHIVir galaxies (M_*^{2D}) versus M_*^{0D} . The comparison is plotted as the logarithmic difference between these two sets of masses [$\log(M_*^{2D}/M_*^{0D})$] as a function of morphology and is carried out for SEDs sampled with the filter combinations gi , giH , $griH$, and $grizH$. Galaxies are ordered from early-types (dE, dS0, E, and S0) on the left, to spirals (Sa–Sm) in the middle, and gas-rich dwarves (Im/BCD) on the right, with dashed lines separating each of these groups. The solid line denotes $M_*^{2D} = M_*^{0D}$ and representative error bars are shown in the bottom-right corner.

using a larger and more complete sample in future work.

2D masses that include NIR information behave similarly to those based on gi bands, except for two important differences: we rarely find positive values of $\log (M_*^{2D}/M_*^{0D})$ and few galaxies cluster about the $M_*^{2D} = M_*^{0D}$ line. The first difference could arise from either an increase in M_*^{0D} or a decrease in M_*^{2D} (or both) as we model more bands than just g and i . Fig. 10 shows that, on average, M_*^{0D} measured from the band combinations giH , $griH$, and $grizH$ are mutually consistent (to within ± 0.03 -5 dex), while gi -based masses are $\sim 13\%$ higher. This behaviour of M_*^{0D} can therefore not explain the observed changes in $\log (M_*^{2D}/M_*^{0D})$; the onus must instead lie with M_*^{2D} . Taking ratios of M_*^{2D} between the datasets considered in Fig. 12 indeed shows that M_*^{2D} typically decreases by $\sim 30\%$ when the SEDs of pixels are sampled with either the giH , $griH$, or $grizH$ filters, compared to the case of gi SEDs. Including NIR fluxes in 2D mass measurements thus systematically reduces galaxy-wide mean M_*/L_i values (as in the 0D case; Fig. 10) and mass maps derived for each of the band combinations gr , gz , and gH confirm that the lattermost yield the smallest values of M_*/L_i per pixel, on average. The discrepancy between optical and optical+NIR masses from our 2D approach supports the suggestion of T11 that predictions of current SPS models lack consistency across the optical-NIR domain. Our own results highlight the need for further tests of the MLCR method (and SPS models in general), preferably on resolved populations, where M_*/L may be directly inferred from colour-magnitude diagrams.

Unlike with our gi -based measurements, the lack of galaxies found in the vicinity of the $M_*^{2D} = M_*^{0D}$ line in Fig. 12 when NIR data are considered implies that 0D values are biased higher than their 2D counterparts in such cases. For early-types and spirals, this bias remains robust amongst the giH , $griH$, and $grizH$ band combinations, falling between -0.05 and -0.07 dex. The bias for gas-rich dwarfs changes significantly between these cases, however, from -0.07 , to -0.09 , and -0.15 dex, respectively. In addition, $\log (M_*^{2D}/M_*^{0D})$ measurements scatter about these median offsets at roughly the 0.04 , 0.05 - 0.06 , and 0.10 - 0.15 dex level for spiral, early-type, and gas-rich dwarf galaxy types. Again though, these estimates must be revisited when larger, homogeneous, and more complete samples of high-quality optical + NIR imaging become available for nearby galaxies. Our experiment with 2D masses that include NIR information thus confirms that the use of integrated photometry increases the random error in associated M_* measurements for whole populations, while introducing a non-trivial bias as well. In the worst case, 0D and 2D masses differ by ~ 0.25 dex when NIR data are involved, and ~ 0.20 dex otherwise.

Fig. 12 can also be compared to Z09 and SS15, the only prior studies of the spatially-resolved approach for measuring M_* . Z09 found that, on a galaxy-by-galaxy basis, M_*^{2D} could exceed M_*^{0D} by as much as ~ 40 - 65% (0.15 - 0.22 dex), depending on the MLCRs and dataset employed; the most egregious disagreements occurred when they modelled optical-to-NIR SEDs. Similarly, SS15 found that, in the most extreme cases, measurements of M_*^{0D} missed ~ 25 , 50 , and 20% of the

stellar mass in E/S0, spiral, and Irr galaxy types. While we find offsets of similar magnitudes to Z09, they only occur in the sense of $M_*^{2D} > M_*^{0D}$ when we consider optical information alone. With NIR fluxes included, our 2D method typically yields smaller masses compared to 0D measurements. A contributing factor might be that the BC03 models tend to predict optical-NIR MLCRs of shallower slopes than the CB07 models (Fig. 8), thereby leading to milder M_*/L gradients. This discrepancy raises further awareness of the need for tests of MLCRs and SPS models on resolved stellar populations; the biased distribution of points in Fig. 12 pertaining to NIR-based predictions strongly hints at a disconnect between SPS models across the optical-NIR domain. However, it should be noted that SS15 measured $M_*^{0D} > M_*^{2D}$ (by as much as 25%) for nearly one-fifth of their full sample, with these galaxies being distinguished by their low-to-medium sSFRs. Recalling that our sample is drawn from a cluster environment and that cluster galaxies tend to exhibit lower sSFRs, relative to their field counterparts, the discrepancies we have uncovered may be genuine.

Aside from some notable outliers, Z09 also argued in favour of a correlation between M_*^{2D}/M_*^{0D} and galaxy type, whereby later-types have larger ratios. They surmised that late-type galaxies, on average, contain more star formation and dust than early-types, hence the integrated light of the former should more often be biased to lower M_*/L . A closer inspection of their Fig. 13 calls some aspects of their claim into question, however. First, the authors do not present any statistical tests for the existence of a correlation (e.g. Spearman’s coefficient) and, second, the correlation disappears when NIR fluxes are included in their modelling. Our own results suggest no such correlation exists for any combination of the SHIVir bands. Instead, our use of a more representative sub-sample of galaxies than Z09’s has demonstrated that the integrated light of all galaxy types, not just late-type spirals, can suffer from significant biases. SS15 also showed (their Fig. 3) that a galaxy’s sSFR appears to be a better diagnostic of these biases. The fact that we recover a dearth of galaxies with $M_*^{2D} > M_*^{0D}$ may be a consequence of this relation and the fact that our sample consists entirely of cluster galaxies. A 2D analysis for a complete sample of galaxies is ultimately needed to establish the dependence of M_*^{2D}/M_*^{0D} .

With a larger, more representative sample of galaxies, we confirm the core results of Z09 and SS15 that M_*^{2D} can M_*^{0D} differ substantially for local galaxies. The degree of scatter seen in Fig. 12 is comparable to that in Fig. 11 for all datasets considered, except *gi* SEDs; M_*^{1D} scatter to a larger degree than M_*^{2D} in this case. These findings appear consistent with the suggestion that radial variations in colour are the predominant cause of differences between spatially-resolved and integrated mass measurements, rather than azimuthal or stochastic (i.e. pixel-by-pixel) variations. However, a larger sample of M_*^{2D} is needed to further test this point. Until such time, our recommendation for the use of M_*^{0D} , M_*^{1D} , or M_*^{2D} depend on the particular application. For accuracies < 0.1 dex and/or small samples, we advocate a spatially-resolved approach (1D/2D), while statistical corrections for the use of integrated light may be invoked in all other cases (see also SS15).

5. Conclusions

Drawing on the literature, SPS models, and a representative sample of local galaxies, we have quantified the random + systematic uncertainties in stellar mass estimates derived from MLCRs. In particular, we have searched for possible biases in M_* due to the use of MLCRs (as opposed to SED fitting), prior assumptions invoked in building MLCRs, scope of SED sampling, and modelling integrated versus spatially-resolved data. Both MLCRs and SED fitting are able to recover the masses of mock galaxies to within ~ 0.2 dex of scatter (even when limited to just g - and i -band photometry), and yield equivalent results when applied to real galaxies. We find that the priors dominate the systematics, contributing at most ~ 0.3 or 0.6 dex of uncertainty, depending on whether optical or optical+NIR photometry is used. Modelling integrated photometry is the next most important effect. In so doing, 0.06 - 0.07 dex of scatter is introduced in M_* measurements, while an additional bias of $+0.05$ - 0.07 dex results from including NIR data. The latter effect may be an indication that SPS models lack consistency throughout the optical-NIR range. From the MLCR perspective, while the use of a single colour (e.g. $g-i$) to constrain M_*/L leads to biases on the order of $\sim 10\%$, increased sampling of galaxy SEDs beyond a few filters spanning the optical-NIR range only serves to reduce the statistical errors in the results.

Our investigation demonstrate that the MLCR and SED fitting methods yield comparable results, as expected since their assessment of M_* both depend on SPS models. Therefore, improvements to the MLCR method should come from extensive analyses of resolved stellar populations in galaxies, whereby fundamental parameters are most accurately constrained via colour-magnitude diagrams. In the meantime, we advocate the use of the MLCR method for applications focussed on exceptionally large datasets and/or complex parameter spaces. Barring future evidence to the contrary, we only recommend the use of a spatially-resolved approach to M_* measurements for cases involving either small numbers of galaxies or if accuracies to better than 0.1 dex are required.

JCR and SC acknowledge financial support from the National Science and Engineering Council of Canada through a post-graduate scholarship and Discovery Grant, respectively. We also thank the referee, Stefano Zibetti, for a very thorough and constructive report, and Michael McDonald for providing the AB photometric zero-points to calibrate our surface brightness profiles extracted from SDSS images.

This research has made use of (i) the NASA/IPAC Extragalactic Data base (NED) which is operated by the Jet Propulsion Laboratory, California Institute of Technology, under contract with the National Aeronautics and Space Administration, as well as NASA’s Astrophysics Data System; and (ii) the Sloan Digital Sky Survey (SDSS). Funding for the creation and distribution of the SDSS Archive has been provided by the Alfred P. Sloan Foundation, the Participating Institutions, the National Aeronautics and Space Administration, the National Science Foundation, the U.S.

Department of Energy, the Japanese Monbukagakusho, and the Max Planck Society. The SDSS Web site is <http://www.sdss.org/>. The SDSS is managed by the Astrophysical Research Consortium (ARC) for the Participating Institutions.

REFERENCES

- Abazajian, K. N., Adelman-McCarthy, J. K., Agüeros, M. A., et al. 2009, *ApJS*, 182, 543
- Behroozi, P. S., Conroy, C., & Wechsler, R. H. 2010, *ApJ*, 717, 379
- Bell, E. F., & de Jong, R. S. 2001, *ApJ*, 550, 212
- Bell, E. F., McIntosh, D. H., Katz, N., & Weinberg, M. D. 2003, *ApJS*, 149, 289
- Bruzual, G., & Charlot, S. 2003, *MNRAS*, 344, 1000
- Bruzual, A. G., 2007, in Vazdekis A., Peletier R. F., eds, *Proc. IAU Symp. 241, Stellar Populations as Building Blocks of Galaxies*. Cambridge University Press, Cambridge, p. 125
- Calzetti, D., Armus, L., Bohlin, R. C., et al. 2000, *ApJ*, 533, 682
- Cappellari, M., & Copin, Y. 2003, *MNRAS*, 342, 345
- Chabrier, G. 2003, *PASP*, 115, 763
- Charlot, S., & Fall, S. M. 2000, *ApJ*, 539, 718
- Conroy, C., Gunn, J. E., & White, M. 2009, *ApJ*, 699, 486
- Conroy, C. 2013, *ARA&A*, 51, 393
- Courteau, S. 1996, *ApJS*, 103, 363
- Courteau, S., Cappellari, M., de Jong, R. S., et al. 2014, *Reviews of Modern Physics*, 86, 47
- da Cunha, E., Charlot, S., & Elbaz, D. 2008, *MNRAS*, 388, 1595
- Gallazzi, A., & Bell, E. F. 2009, *ApJS*, 185, 253
- Gallazzi, A., Charlot, S., Brinchmann, J., White, S. D. M., & Tremonti, C. A. 2005, *MNRAS*, 362, 41
- Gavazzi, G., Boselli, A., Donati, A., Franzetti, P., & Scodreggio, M. 2003, *A&A*, 400, 451
- Hall, M., Courteau, S., Dutton, A. A., McDonald, M., & Zhu, Y. 2012, *MNRAS*, 425, 2741
- Into, T., & Portinari, L. 2013, *MNRAS*, 430, 2715
- Longhetti, M., & Saracco, P. 2009, *MNRAS*, 394, 774
- Mannucci, F., Cresci, G., Maiolino, R., Marconi, A., & Gnerucci, A. 2010, *MNRAS*, 408, 2115

- Maraston, C. 2005, MNRAS, 362, 799
- Marigo, P., & Girardi, L. 2007, A&A, 469, 239
- Marigo, P., Girardi, L., Bressan, A., et al. 2008, A&A, 482, 883
- Mei, S., et al. 2007, ApJ, 655, 144
- McDonald, M., Courteau, S., & Tully, R. B. 2009, MNRAS, 394, 2022
- McDonald, M., Courteau, S., Tully, R. B., & Roediger, J. 2011, MNRAS, 414, 2055
- McGaugh, S. S., & Schombert, J. M. 2014, AJ, 148, 77
- Roediger, J. C., Courteau, S., McDonald, M., & MacArthur, L. A. 2011, MNRAS, 416, 1983
- Schlafly, E. F., & Finkbeiner, D. P. 2011, ApJ, 737, 103
- Schlegel, D. J., Finkbeiner, D. P., & Davis, M. 1998, ApJ, 500, 525
- Skrutskie, M. F., et al. 2006, AJ, 131, 1163
- Sorba, R., & Sawicki, M. 2015, arXiv:1506.01653
- Taylor, E. N., Hopkins, A. M., Baldry, I. K., et al. 2011, MNRAS, 418, 1587
- Tremonti, C. A., Heckman, T. M., Kauffmann, G., et al. 2004, ApJ, 613, 898
- van Albada, T. S., & Sancisi, R. 1986, Royal Society of London Philosophical Transactions Series A, 320, 447
- van Dokkum, P. G. 2008, ApJ, 674, 29
- Zibetti, S. 2009, arXiv:0911.4956
- Zibetti, S., Charlot, S., & Rix, H.-W. 2009, MNRAS, 400, 1181

A. Appendix

Table 2 provides linear least-squares fits to the MLCRs created on the basis of the BC03 and FSPS SPS models (see Figs. 7-8). Fits are provided for each of the filter and colour combinations accessed by our dataset. The coefficients in this table follow the generic equation: $\log(M_*/L)_\lambda = m_\lambda \times (colour) + b_\lambda$. We omit the CB07 MLCRs as those can be found in Table B1 of Z09. Table 3 shows the Pearson correlation coefficient for each of these fits. In all cases the coefficient is greater than 0.55, and $\sim 70\%$ of the time it is greater than 0.85.

Table 2. Coefficients of linear fits for the BC03 and FSPS MLCRs.

Colour (1)	m_g (2)	b_g (3)	m_r (4)	b_r (5)	m_i (6)	b_i (7)	m_z (8)	b_z (9)	m_H (10)	b_H (11)
BC03:										
$g-r$	2.029	-0.984	1.629	-0.792	1.438	-0.771	1.306	-0.796	0.980	-0.920
$g-i$	1.379	-1.067	1.110	-0.861	0.979	-0.831	0.886	-0.848	0.656	-0.950
$g-z$	1.116	-1.132	0.900	-0.916	0.793	-0.878	0.716	-0.888	0.521	-0.968
$g-H$	0.713	-1.070	0.577	-0.870	0.507	-0.834	0.454	-0.842	0.313	-0.902
$r-i$	4.107	-1.170	3.325	-0.952	2.925	-0.908	2.634	-0.912	1.892	-0.977
$r-z$	2.322	-1.211	1.883	-0.987	1.655	-0.937	1.483	-0.935	1.038	-0.975
$r-H$	1.000	-0.988	0.814	-0.809	0.713	-0.778	0.634	-0.786	0.414	-0.833
$i-z$	5.164	-1.212	4.201	-0.991	3.683	-0.939	3.283	-0.931	2.210	-0.947
$i-H$	1.257	-0.869	1.024	-0.713	0.895	-0.693	0.792	-0.706	0.495	-0.761
$z-H$	1.615	-0.729	1.316	-0.600	1.150	-0.593	1.015	-0.616	0.615	-0.692
FSPS:										
$g-r$	1.897	-0.811	1.497	-0.647	1.281	-0.602	1.102	-0.583	0.672	-0.605
$g-i$	1.231	-0.805	0.973	-0.644	0.831	-0.597	0.713	-0.576	0.426	-0.592
$g-z$	0.942	-0.764	0.744	-0.612	0.634	-0.568	0.542	-0.548	0.316	-0.565
$g-H$	0.591	-0.655	0.468	-0.527	0.398	-0.494	0.339	-0.482	0.191	-0.515
$r-i$	3.374	-0.745	2.675	-0.600	2.275	-0.556	1.940	-0.537	1.120	-0.554
$r-z$	1.795	-0.670	1.421	-0.539	1.206	-0.502	1.021	-0.487	0.570	-0.513
$r-H$	0.824	-0.542	0.654	-0.439	0.555	-0.418	0.469	-0.414	0.254	-0.463
$i-z$	3.709	-0.550	2.933	-0.443	2.484	-0.419	2.084	-0.411	1.112	-0.457
$i-H$	1.073	-0.460	0.852	-0.375	0.722	-0.362	0.608	-0.365	0.322	-0.430
$z-H$	1.493	-0.414	1.188	-0.339	1.008	-0.333	0.849	-0.341	0.449	-0.417

Table 3. Pearson correlation coefficients for the BC03 and FSPS MLCRs.

Colour (1)	r_g (2)	r_r (3)	r_i (4)	r_z (5)	r_H (6)
BC03:					
$g-r$	0.98	0.97	0.96	0.96	0.92
$g-i$	0.99	0.98	0.97	0.97	0.91
$g-z$	0.98	0.98	0.97	0.96	0.89
$g-H$	0.95	0.95	0.94	0.93	0.82
$r-i$	0.98	0.97	0.97	0.96	0.88
$r-z$	0.96	0.96	0.95	0.94	0.84
$r-H$	0.90	0.90	0.89	0.87	0.72
$i-z$	0.92	0.92	0.91	0.90	0.77
$i-H$	0.85	0.85	0.84	0.82	0.65
$z-H$	0.81	0.82	0.80	0.78	0.60
FSPS:					
$g-r$	0.95	0.93	0.91	0.88	0.74
$g-i$	0.96	0.93	0.91	0.88	0.73
$g-z$	0.95	0.93	0.91	0.87	0.70
$g-H$	0.94	0.92	0.90	0.86	0.66
$r-i$	0.94	0.92	0.90	0.86	0.69
$r-z$	0.93	0.91	0.88	0.84	0.65
$r-H$	0.91	0.90	0.87	0.83	0.62
$i-z$	0.90	0.88	0.85	0.80	0.59
$i-H$	0.90	0.88	0.85	0.81	0.59
$z-H$	0.89	0.88	0.85	0.81	0.59